Carnegie Mellon University

CARNEGIE INSTITUTE OF TECHNOLOGY

THESIS

SUBMITTED IN PARTIAL FULFILLMENT OF THE REQUIREMENTS

FOR THE DEGREE OF Doctor of Philosophy

TITLE **Automatic Common Carotid Artery and Internal Jugular Vein Identification and Tracking for the Sonic Flashlight**

PRESENTED BY **David C. Wang**

ACCEPTED BY THE DEPARTMENT OF

Biomedical Engineering

George D. Stetten, ADVISOR, MAJOR PROFESSOR — DATE

Todd M. Przybycien, DEPARTMENT HEAD — DATE

APPROVED BY THE COLLEGE COUNCIL

DEAN — DATE

Automatic Common Carotid Artery and Internal Jugular Vein Identification and Tracking for the Sonic Flashlight

David C. Wang

CMU-BME
Version 2.0
May 09, 2007

Department of Biomedical Engineering
Carnegie Mellon University
Pittsburgh, PA 15213

Submitted in partial fulfillment of the requirements
for the Degree of Doctor of Philosophy

Thesis Committee
Dr. George Stetten (BME and Thesis Advisor)
Dr. Jelena Kovacevic (BME)
Dr. Lee Weiss (BME)
Dr. Roberta Klatzky (external)

This research was supported by NIH Grant R01-EB00860 and R01-HL074285-01

Keywords

Bioengineering, Biomedical Engineering, Central Venous Access, Common Carotid Artery, Image Analysis, Internal Jugular Vein, Peripherally Inserted Central Catheter, Real-Time Tomographic Reflection, Sonic Flashlight, Ultrasonography, Ultrasound

Abstract

We have built a fully automated ultrasound analysis system that tracks and identifies the common carotid artery (CCA) and the internal jugular vein (IJV). The system is intended to be used in conjunction with the Sonic Flashlight (SF), an augmented reality device that provides real-time *in* situ visualization of ultrasound images by reflecting calibrated images into a patient's body. Our goal is to prevent inadvertent damage to the CCA when targeting the IJV for catheterization. The automated system starts by identifying and fitting ellipses to all the regions that look like major arteries or veins throughout each B-mode ultrasound image frame. The *Spokes Ellipse* algorithm described in this thesis tracks these putative vessels and calculates their characteristics, which are then weighted and summed to identify the vessels. The optimum subset of characteristics and their weights were determined from a training set of 38 subjects, whose necks were scanned with a portable 10 MHz ultrasound system at 10 fps. Wilks' Lambda analysis narrowed the characteristics to the five that best distinguish between the CCA and IJV. A paired version of Fisher's linear discriminant analysis was used to calculate the weights for each of the five parameters. Leave-one-out validation studies showed that the system could track and identify the CCA and IJV with 100% accuracy in this data set. The system's limitations and future work are also discussed in this thesis.

Acknowledgments

Thanks are first due to my committee, Dr. George Stetten, Dr. Jelena Kovacevic, Dr. Lee Weiss, and Dr. Roberta Klatzky, for their help in carrying out this project, and the significant insights I gained from their own work.

Dr. George Stetten invented the Sonic Flashlight, and I was given the opportunity to be in charge of developing a new generation of the device as well as carrying out its clinical trials. Much of the motivation for this thesis derived from ideas related to the Sonic Flashlight. He also did the extensive editing of all my papers to the point of driving him to call me a "slave driver." Dr. Jelena Kovacevic's class on wavelet theories inspired my work on vascular image analysis. Dr. Lee Weiss contributed the idea of displaying the confidence level of the final vessel determinations. Dr. Roberta Klatzky was my frequent consultant on all things statistical - from experimental design to data analysis.

Thanks are also due to other members of Vialab – Dr. Nikhil Amesur, Dr. Wilson Chang, Dr. Bing Wu, Dr. Robert Tamburo, Dr. (soon to be) Aaron Cois, Dr. Damion Shelton, Ken Rockot, Dr. (soon to be) John Galeotti, Dr. (in a few years) Gaurav Shukla, David Weiser, and Dr. (in a few years) Sam Clanton.

Dr. Nikhil Amesur is an interventional radiologist who contributed many ideas to make the Sonic Flashlight useful clinically. Dr. Wilson Chang carried out the initial prototyping work of the Sonic Flashlight. Dr. Bing Wu took care of analyzing how people perceive images through the Sonic Flashlight. Dr. Robert Tamburo, Aaron Cois, Dr. Damion Shelton, and Ken Rockot gave me tremendous assistance in using the Insight Toolkit software for real-time image analysis. John Galeotti and I motivated each other to work out and keep ourselves in healthy shape. Gaurav Shukla assisted in obtaining clinical trial approvals from the Institutional Review Board and will continue developing and testing the Sonic Flashlight when I leave. David Weiser made many of the engineering designs a reality. Finally, Sam Clanton introduced me to the world of robotics with the tele-painter project.

I would also like to thank Dr. Sampson from the statistics department for helping to validate the paired linear discriminant analysis methods used in classifying vessels based on training data.

Lastly, I would like to thank my parents, Soo-Ray and Sharon, and my siblings, Amy and Richard, who have been a steady source of support and encouragement, but who will probably be relieved when I finally return to medical school.

Table of Contents

List of Abbreviations

CCA	common carotid artery
IJV	internal jugular vein
PICC	peripherally inserted central catheter
RTTR	real-time tomographic reflection
SF	Sonic Flashlight
cpm	cycles per minute
fps	frames per second

List of Tables

List of Illustrations

Chapter 1. Introduction

Ever since Wilhelm Roentgen took the famous x-ray image of a hand in 1896, medical professionals have become increasingly dependent on imaging technologies to see inside a patient. Advances in medical imaging exploded with the advent of the computer age, allowing researchers to develop new imaging modalities, automated image analysis techniques, augmented reality displays, etc. The work described here combines a number of these avenues in medical imaging to automatically analyze ultrasound image in real-time and place it as a virtual image inside a patient at the same location where the image is being acquired. The ultimate goal is to allow the operator to see the patient's internal anatomy, appropriately identified, floating inside a patient in real time.

This thesis makes contributions in the development of algorithms for automated vessel analysis, and especially in a novel quantitative analysis of the phase difference between the common carotid artery (CCA) and internal jugular vein (IJV). We begin in Chapter 2 with a brief introduction to ultrasonography followed by Chapter 3 with an introduction to the Sonic Flashlight (SF) – a new method of ultrasound image display that I have helped develop and test throughout my PhD training. Chapter 4 describes the targets of my analysis, the CCA and the IJV. 5.2 describes the *Spokes Ellipse* algorithm that I invented. The rest of the thesis deals primarily with the development and implementation of a real-time automated system for identifying the CCA and IJV. My other SF-related research as well the raw data from the thesis are presented in the Appendix.

Chapter 2. Ultrasonography

2.1. Physics

Ultrasound is acoustic energy with a frequency greater than the upper limit of human hearing - approximately 20 kHz [53]. Ultrasonography is a medical imaging technique that uses high frequency sound waves and their echoes. The technique is similar to the echolocation used by bats, whales and dolphins, as well as SONAR used by submarines. The ultrasound probe transmits high-frequency (3 to 13 megahertz) sound pulses into a patient's body using an array of piezoelectric elements. The sound waves travel into the body and are reflected by discontinuities in acoustic impedance between tissues (e.g. between fluid and soft tissue, soft tissue and bone) as well as by impedance inhomogeneities within tissues. One particular form of inhomogeneity, smaller than the resolution of the ultrasound, causes pseudorandom variation in the resulting image known as "speckle". Some of the sound waves may thus be reflected back to the probe at a given depth, while some travel on further until they reach another boundary where more may be reflected. The reflected waves are picked up by the probe and used to calculate the distance from the probe to the tissue or organ (boundaries), using the speed of sound in tissue (approximately 5,005 ft/s or1,540 m/s) and the time of each echo's return. The scanner displays the distances and intensities of the echoes on a screen, forming a two dimensional image. In a typical ultrasound scanner, thousands of pulses and echoes are sent and received each second by a phased array of transducer elements, which can steer these interrogations across a plane to form an image at rates of 10-30 frames/sec. The probe can be moved in real time along the surface of the body and angled to obtain various views.

2.2. Ultrasound Image Analysis

Due in part to the presence of speckle, ultrasound is among the noisiest of all medical imaging modalities, and its anisotropy and path dependence add further difficulties for automated image analysis. Many researchers have developed ultrasound tracking techniques. Abolmaesumi et al., described methods to automatically track and segment the boundary of the CCA using the "Star" algorithm, stabilized by a temporal Kalman filter [14]. However, it requires initialization using prior knowledge about probe movement. Yeung et al., showed that objects in sequential ultrasound images can be tracked using a deformable mesh model [15], but not in real-time. Nakayama et al., designed an ultrasonic method of measuring arterial wall movement [16], but it requires manual outlining of the vessels and scanning in longitudinal section rather than cross section. Wilson described methods using Doppler to automatically recognize the walls of a blood vessel and determine its orientation and diameter [17]. None of these methods deals directly with identifying the blood vessels or differentiating artery from vein.

Methods to identify anatomical targets other than vascular structures have also been investigated. Drukker et al., researched the use of a radial gradient index filter to automatically detect lesions in breast ultrasound [18]. Ladak et al., developed automatic methods to segment the boundaries of the prostate [19]. Algorithms also exist for automatically locating instruments such as biopsy needles in an ultrasound image [20]. The above list is not meant to be all-inclusive. Many researchers have applied image analysis to clinical ultrasound, but to our knowledge, our system is the first to automatically identify and differentiate between vascular structures, namely, the CCA and IJV.

Chapter 3. The Sonic Flashlight

Ultrasound is widely used in current practice for guiding needle insertions into anatomical objects hidden under the skin, such as veins and tumors. However, the operator typically must look away at a separate video monitor and mentally construct the interaction between the ultrasound transducer, the needle, and the anatomical target object. We believe our Sonic Flashlight (SF) solves the problem of this displaced sense of hand-eye coordination by combining all elements into a single 3D visual environment.

3.1. Real Time Tomographic Reflection

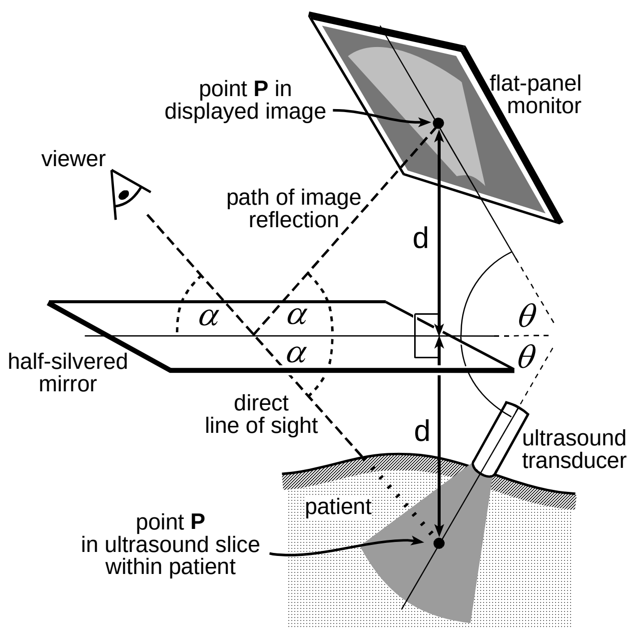

Figure 1. Geometric relationships for Real Time Tomographic Reflection.
The mirror must bisect the angle between the slice and the monitor, with both sub-angles sharing a common vertex. On the monitor, the image must be correctly scaled, translated and rotated so that each point in the image is paired with its corresponding point in the slice to define a line segment perpendicular to, and bisected by, the mirror. By fundamental laws of optics, the ultrasound image will appear at its physical location, independent of viewer position

The approach developed in our laboratory is shown in Figure 1. An ultrasound scanner acquires a tomographic slice representing a set of 3D voxels in a plane. The image of that slice, displayed at its correct size on a flat panel display, is reflected to occupy the same physical space as the slice within the patient. The patient is viewed through a beam-splitter (half-silvered mirror) with the reflected image correctly located, independent of viewer location. Since the ultrasound scanner is an integral part of the apparatus, no tracking of the patient is required, setting it apart from other approaches that each depend on some form of tracking and head-mounted device that the operator must wear [21-24]. Given that ultrasound is a real-time modality, the image will change, for example, during an invasive procedure, to show the results of the procedure. We have adopted the term *Real Time Tomographic Reflection* to convey this concept [25-30].

In Figure 2, a transducer is pressed against the right side of a human neck. The structures in the ultrasound image (CCA and IJV) are located consistent with external surface of the neck. The photograph cannot convey the strong sense, derived from stereoscopic vision, that the reflected image is located within the neck. This sense is intensified by head motion, because the image remains properly aligned from different viewpoints. To one experiencing the technique in person, ultrasound targets within the neck are clearly accessible to direct percutaneous needle placement. We have named the device the Sonic Flashlight (SF) because the transducer appears to illuminate the interior of the patient with the ultrasound data.

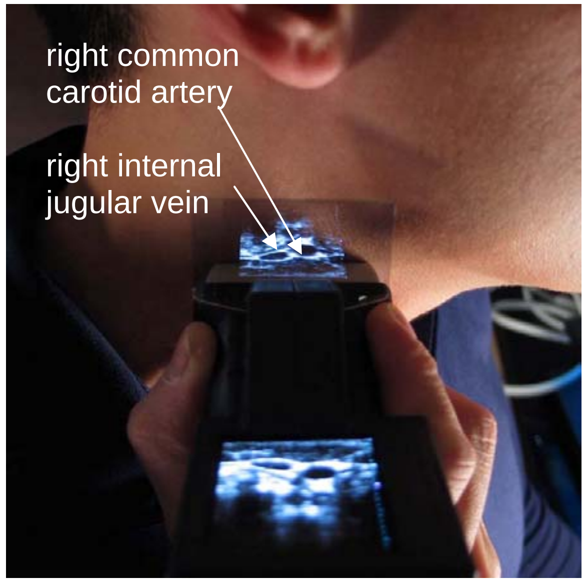

Figure 2. View of vessels in the neck through the half-silvered mirror of the SF

3.2. Device Specification

The particular model of the SF used throughout this thesis consists of a 10MHz ultrasound system (Terason, Burlington, MA) whose probe is fitted with a small flat-panel display (AM550L OLED, Kodak, Rochester, NY). Unlike previous models, we designed this model for sterile clinical use and thus it does not contain a dedicated mirror (Figure 3) [48]. A standard sterile clear probe cover (BARD, Murray Hill, NJ) is fitted over the probe and the display. A disposable sterile mirror holder with a 20x50x2mm half-reflective/transparent plastic mirror is then fitted outside the cover, pressing the cover flat against the display (Figure 4).

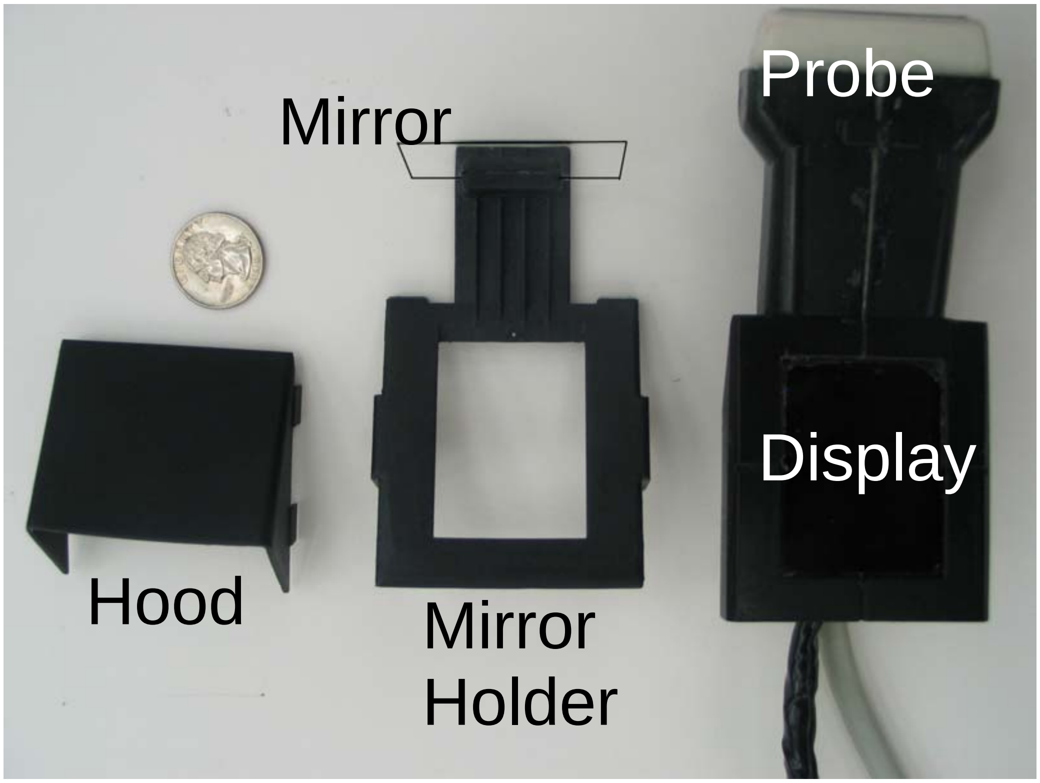

Figure 3. The three components of the Sonic Flashlight – the hood, the mirror holder, and the base consisting of an OLED display and an ultrasound transducer.

Figure 4. The fully assembled Sonic Flashlight with the plastic probe cover bag enveloping only the base.

3.3. Psychophysical Studies

Over the past four years, in collaboration with Dr. Roberta Klatzky and post-doctoral fellow Dr. Bing Wu in the Department of Psychology at CMU, our laboratory has explored the psychophysics of the SF in depth [61,62,67-71]. These psychophysical studies have found that even untrained users of the SF show natural facility with its use. One set of experiments [67-68] assessed first-time users' ability to localize targets, by having them point from the surface of a phantom, and also tracked a needle as they guided it to the target location. Users of the SF perceive target depth comparably to direct vision of the target in a transparent phantom, whereas CUS users systematically aim too shallow. Likely reasons are that they underestimate distances defined in standard units (inches or centimeters) on the CUS screen and fail to compensate for indentation of the phantom surface. These errors do not affect the SF, as perceived target location is unchanged by indentation of the phantom and does not depend on knowledge of arbitrary units of distance [69-70]. Sub-specialty experts compensate for tissue compliance by keeping the needle in-plane, where they can home in on the target. But when through-plane needle trajectories are advantageous for reasons such as seeing the cross sectional area of blood vessels, the superior accuracy of the SF on compliant tissues may have important clinical significance. Clearly, these are promising areas of psychophysical research that may lead to a better understanding of the SF and possibly of human perception and motor function in general.

3.4. Clinical Trials

Our first clinical trials with the SF involve placing Peripherally Inserted Central Catheter (PICC) lines in the arm. These are considered one of the safest vascular catheter placement procedures. As such, they are preferable to direct central lines such as in the jugular vein for our initial clinical trials. They are also the only vascular catheter placement that nurses are approved to perform at the patient's bedside. All others must be performed by doctors.

We have used the SF to successfully place PICC lines in 70 patients – 26 in the radiology operating suites by an interventional radiologist followed by 44 at the bedside by two nurses from the intravenous team. All 3 operators had gone through a brief period of training before the clinical trials. All the subjects were recruited from patients at the University of Pittsburgh Medical Center Presbyterian Hospital who had an order from their doctor to have a PICC line placed.

The procedures began with the operator scanning the patient's upper arm with both the SF and CUS. To avoid variability between different ultrasound systems, we used the same Terason ultrasound probe with its unaltered laptop-based display as the CUS for comparison. Identification of the basilic vein, brachial vein, and brachial artery with each modality were recorded. If the basilic vein was visualized using the SF, the SF was used to guide a needle (21 gauge, 7cm) into the basilic vein. The basilic vein was prefered since it is further from other critical structures in the arm, reducing the risk of complications. If the basilic vein was determined to be an inappropriate target, the brachial vein would be used instead. If vascular access was unsuccessful after three attempts with the SF, the operator would revert to using CUS for the procedure. If successful access was gained in the selected vein, the procedure would continue as in a standard PICC line procedure.

In all of the subjects, the vessels were visualized in situ using the SF. The needle was easily aimed and inserted into the basilic or brachial vein. Successful access was obtained in all of them. With the first 15 patients, we were using a previous model of the sonic flashlight without the removable mirror assembly described above. Because this model required the mirror to be inside the sterile bag, the interventional radiologist noticed an image distortion problem in 3 of the procedures. This prompted an extensive re-engineering effort described in Appendix A, resulting in our current design with the disposable mirror assembly outside the bag.

After resolving the image distortion problem, the remaining cases proceeded successfully with their procedures in the hands of nurses in addition to the radiologist. The performances of the operators are listed in Table 1, which also shows several days of self-reported performances from the two nurses prior to their commencing the SF studies. The data shows that there is no significant difference in performance attributable to the re-engineered SF. There is also no evidence of a difference between the SF and the CUS for either nurse. This may be due to a ceiling effect because both nurses already have more than 10 years of experience placing PICC lines, and they are proficient at what they do no matter which display modality they use.

The only conclusion we can make thus far with the radiologist and experienced nurses is that the operators were all able to adapt quickly to the SF without performance decrement, and possibly with performance improvement. In fact, Nurse 2 stated that she was able to insert the needle more parallel to the skin than before. With the CUS, she normally presses down perpendicularly on the skin with the needle cap until she sees the vein compress on ultrasound. The path of such compression represents her planned trajectory for her needle. With the SF, she no longer needed such trajectory planning, and could insert into the vein at arbitrary angles.

Table 1. Number of Needle Punctures before Venous Access is Achieved

Operator	Modality	1 puncture	2 punctures	>3 punctures	Chi-Square
Radiologist	Old SF	13	2	0	1.613
	SF	8	2	1	
Nurse 1	CUS	29	1	0	2.17
	SF	19	0	1	
Nurse 2	CUS	23	3	4	2.59
	SF	14	5	1	

*Old SF refers to the version before the re-engineering (see text)

** For p<0.05, the significance threshold for the chi-square is >5.99

We may see greater difference in upcoming PICC line trials by nurses with less experience. Alongside the planned continuation of PICC line trials, we are also planning the use of the SF to include other central venous access catheter placement sites such as the IJV in the neck, the subclavian veins in the shoulder, and the femoral veins in the groin. We have also conducted a preliminary trial for breast tumor biopsy, and plan to extend this with design of a special SF for this new application.

3.5. Motivation from the Sonic Flashlight

Since the SF scales images to the actual size of their underlying structures, vessels can appear quite tiny to the naked human eye. These targets are, after all, often on the order of millimeters, and ultrasound operators are used to seeing them magnified on the scanner display. It is therefore necessary to enhance the SF image in such a way that allows the naked human eye to unambiguously identify and locate the appropriate vessels. Solving this problem evolved into my thesis work of building an automated vessel tracking and identification system. With future clinical trials for central line placement in mind, we have decided to focus on CCA and IJV tracking and identification, because mistakes in their identification can carry the gravest consequences as described in Chapter 4.

By using the SF instead of the conventional ultrasound machine, we believe the operator can already more accurately and easily determine the spatial location of the CCA and IJV. This can help the operator in puncturing only the IJV and not the CCA. We believe an automated vessel identification system operating in real time during the procedure could further decrease the incidence of inadvertent CCA puncture and expedite needle insertion. By analyzing the properties of the tracked objects, it should be possible to automatically classify and graphically mark each as an artery, vein, or other tissue type, with the markings being displayed by the SF superimposed on the ultrasound image, floating within the patient. Such markings could obviously be used with conventional ultrasound displays as well. In either case, this could help prevent the operator, especially the relative novice, from accidentally puncturing the CCA.

3.6. Related Extensions of the SF

A number of related extensions of the RTTR concept underlying the SF have been pursued by others in our laboratory. Using a prototype Real Time 3D (matrix array) ultrasound scanner, the first C-Mode SF was built, displaying a slice parallel to the face of the transducer at a constant depth below the skin [55-56]. A miniature SF, called the *sonic penlight*, was constructed for use with surgical “loupes” (magnifying glasses) to guide procedures close to the skin, such as tendon surgery and pediatric vascular access [57]. I was involved in developing a laser guidance system attached to a needle to permit the operator to “home in” on targets in the virtual image of the SF (See Appendix) [58]. I also helped explore an extension of the underlying concept of RTTR to robotic catheter-based systems and microscopy, resulting in a number of working prototypes (See Appendix) [59-60]. A virtual SF system has been constructed by others in my lab, using tracking to provide simulated targets for psychophysical testing [62]. And finally, our lab is developing a version of the SF with the half-silvered mirror replaced by a holographic plate, to produce larger virtual images without compromising the inherent flexibility and ease of use afforded by the small size and weight of the mirror-based SF [63-66].

Chapter 4. The Common Carotid Artery and Internal Jugular Vein

The CCA and the IJV run side-by-side in the neck, one pair on the left and one on the right as shown in Figure 5 [31]. The CCA carries oxygenated blood up to the head while the IJV drains deoxygenated blood down to the heart. The right IJV is a common entry site for intravascular procedures such as central catheter line placement, hemodynamic measurement, myocardial biopsy, cardiac ablation, etc. The right IJV is chosen because its path to the right atrium is straighter than that from the left IJV.

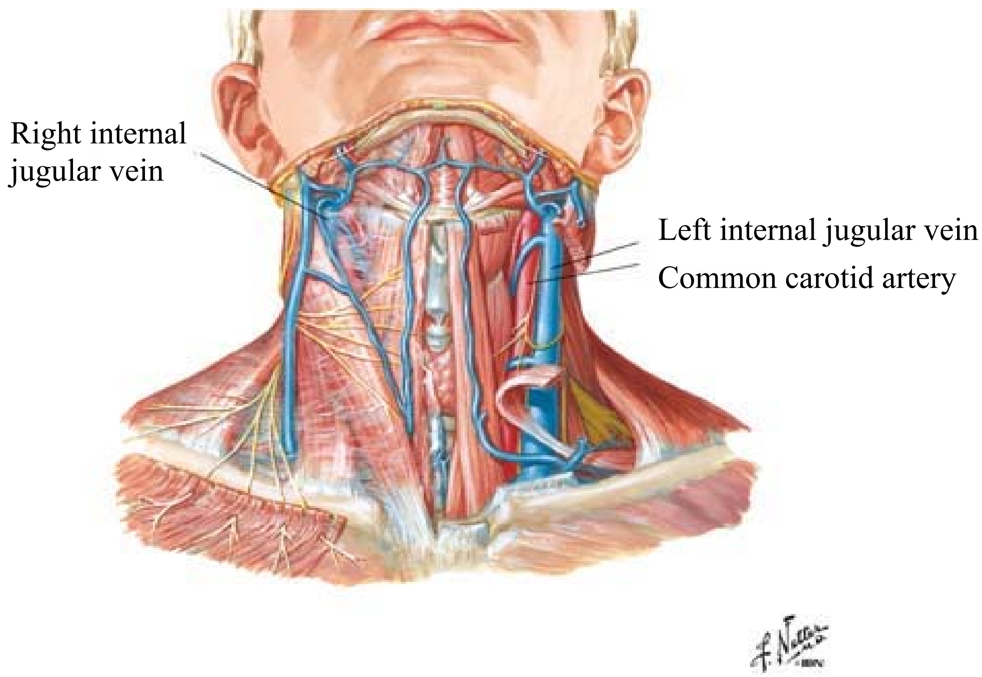

Figure 5. Anatomy of the neck

4.1. Physiology of normal vasculature

Blood vessels are generally divided into 5 categories, in order of blood flow from the heart: arteries, arterioles, capillaries, venules, and veins. The CCA and the IJV belong to the largest class of arteries and veins, respectively, in the human body. The walls (outer structure) of arteries consist of three layers including a layer of smooth muscle fibers that contract and relax under the instructions of the sympathetic nervous system. The corresponding three layers of a vein are thinner and less elastic. Table 2 shows a comparison between arteries and veins.

Table 2. General comparison between arteries and veins.

Arteries	**Veins**
Transport blood away from the heart	Transport blood towards the heart
Carry oxygenated blood (except in the case of the pulmonary artery)	Carry de-oxygenated blood (except in the case of the pulmonary vein)
Have relatively narrow lumens	Have relatively wide lumens
Have relatively more muscle/elastic tissue	Have relatively less muscle/elastic tissue
Transport blood under higher pressure	Transport blood under lower pressure
Do not have valves (except for the semi-lunar valves of the pulmonary artery and the aorta)	Have valves throughout the main veins of the body. These are to prevent blood flowing in the wrong direction.

4.2. Pulsatile motion of the Common Carotid Artery and Internal Jugular Vein

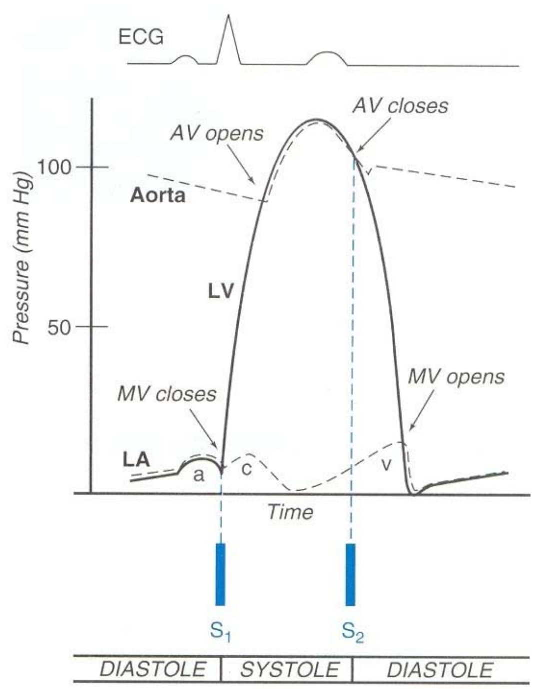

Figure 6. Variations in the aorta and left atrium within a cardiac cycle [32].

The beating heart and to a lesser extent, the movement of the lungs, contribute to the pulsations in the CCA and IJV. The heart affects them by varying the flow of blood while the lung affects them through external compressions on the vessels. While the lung can be expected to affect the two vessels equivalently, the beating heart's effects on the hemodynamics of the CCA and IJV differ in a consistent manner. The CCA experiences the highest blood pressure when the left ventricle contracts, causing a surge of blood to flow into the CCA through the aorta. The IJV experiences the highest blood pressure when the right atrium contracts, regurgitating blood to the IJV through the superior vena cava. Since the atria and ventricles do not contract simultaneously, the pulsations of the

CCA and IJV are consistently out of phase in a given cardiac cycle.

The pulsation of the CCA, which branches off the aorta, mimics that of the aorta shown in Figure 6 [32]. Its pressure peaks when the left ventricle contracts, just before the aortic valve (AV) closes to produce the second heart sound (S2). The right atrial contractions cause increased pressures in the superior vena cava, creating a corresponding peak in IJV pressure. Thus, the pressure of the IJV peaks just before the first heart sound (S1) as shown in Figure 7 [33]. Since the pressures in the CCA and IJV depend on the timing of contractions of the ventricle and atrium, respectively, we should expect a phase difference between the pulsations in the CCA and the IJV.

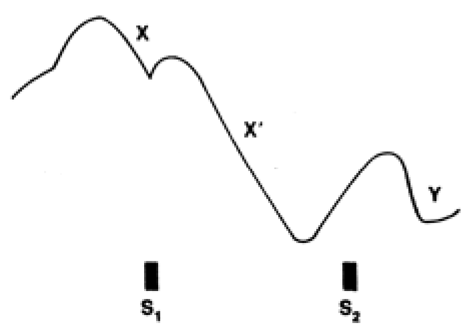

Figure 7. Pressure variations in the internal jugular vein within a cardiac cycle. S1 and S2 refer to the first and second heart sounds, respectively. X, X', and Y descents occur due to interactions between the various contracting and relaxing atriums and ventricles.

4.3. Difficulties with Catheterization of the IJV

The most common serious complication of inserting a needle into the IJV is inadvertent CCA puncture, reported to have an incidence of 2-8% [1][2] and usually resulting in localized hematoma formation. The hematoma may enlarge rapidly if the patient is on any anti-coagulation regimen, has a naturally occurring problem with clotting, or if a large puncture wound is produced by the introduction of the sheath itself into the carotid artery. Airway obstruction [3][4], pseudoaneurysm [5][6], arterio-venous fistula formation [7], and retrograde aortic dissection [8] have all been reported as a consequence of carotid puncture. In the presence of occlusive (atheromatous) carotid disease, inadvertent puncture may carry the risk of precipitating a cerebrovascular accident [9] with potentially fatal consequences.

The most important factor in inadvertent CCA punctures during needle insertion into the IJV is usually the anatomical relationships between the CCA and IJV. Normally the IJV is anterolateral to the CCA, with minimal overlap. However, this relationship is lost when the head is rotated away from the midline, a technique commonly used to facilitate exposure of the IJV prior to needle insertion. As the head is rotated more than 40^{o} from midline, the percent overlap of the CCA and IJV increases significantly [10]. Since it is very common for needles to penetrate the back wall of a vessel after penetrating the more superficial wall, any structure behind the target vessel is at risk of being punctured. Thus, the greater the overlap between the CCA and IJV, the greater is the risk of inadvertent puncture of the CCA. Aberrant anatomic relationships between the IJV and CCA have also been observed in as many as 3% of adult patients studied by ultrasound when their heads are rotated 30^{o} from midline [11]. In 2% of the adult patients the IJV was positioned contrary to normal anatomy, medial to the carotid artery, and the CCA coursed posteriorly to the IJV in 10% of pediatric cardiac patients [12]. Thus it is critical to develop a method to clearly identify and mark the CCA and IJV without depending on normal anatomical relationships.

The introduction of B-mode ultrasound to guide IJV access has decreased the arterial puncture incidence [13]. However, the appearances of CCA and IJV are still very similar in B-mode ultrasound – both appear as hypoechoic pulsating ellipses. The direction and pattern of flow from color Doppler can further help distinguish arteries from veins, but doctors generally hold the ultrasound transducer perpendicular to the target vessels during vascular access, whereupon slight angular deviation may reverse the perceived direction of flow (Doppler can only sense towards or away from the transducer), making identification of the vessels ambiguous. Thus color Doppler is generally only used during pre-operative evaluation and not during the actual procedure.

In the chapters that follow, we will describe methods of analysis for ultrasound images from the neck that identify the CCA and IJV.

Chapter 5. *Spokes Ellipse* Algorithm

5.1. *Overview*

We have developed an efficient algorithm that tracks blood vessels in real time and simultaneously calculates their elliptical radii and cross sectional area in each frame to be used in vessel classification [34,35]. The *Spokes Ellipse* algorithm outlines and tracks the vessel walls in a sequence of frames (Figure 8), given an initialization process described in the next section. Much like the above-mentioned “Star” algorithm, the *Spokes Ellipse* algorithm initially draws radial lines emanating from a seed point. An intensity-based boundary detection algorithm searches for the most likely boundary along each spoke. Spokes that are too short or too long with respect to the other spokes are eliminated. From the remaining spokes, an ellipse is fitted by a least squares method [36]. The cross sectional area of the vessel is approximated by the area of the ellipse. The center of the ellipse is then used as the seed point for the spokes in the next frame. By recalculating the center of the vessel and its boundaries in each frame, the vessel can be tracked in real-time, although sudden movement of the transducer may cause the tracking to be lost. This algorithm is run twice in each frame, since there are two vessels to track: the CCA and the IJV.

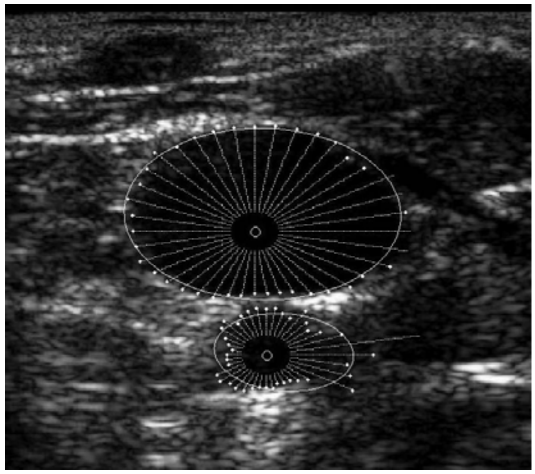

Figure 8. *Spokes ellipse* algorithm applied to the IJV (top) and the CCA (bottom). Spokes grow until they reach a boundary (white dots) or a pre-set maximum length (lines without a dot at the end). Ellipses are fit to the dots for each vessel. Algorithm runs in real time.

5.2. Data Acquisition

We briefly summarize here how those images were obtained.

5.2.1. Device Specifications

The ultrasound machine we have chosen to capture images of the CCA and IJV is the same ultrasound system upon which the current clinical SF has been built: a portable linear 10MHz system (Terason 2000, Terason, Burlington, MA) operating on a Dell Latitude C840 laptop. The transducer (10L5) is a linear wideband 128 element probe. Ultrasound images were transferred in real time via USB 2.0 to an external hard drive at 10 fps. Each frame is 512 pixels by 512 pixels stored as 8-bit grey-scale tiff format files without compression. Depth and width of scan were both set to approximately 5cm.

5.2.2. *Subject Recruitment*

We recruited 42 healthy volunteers ages 20 to 51. The volunteers were asked to lie supine with their heads turned to the left. The right sides of their necks were scanned with ultrasound in the standard manner. A series of digitized images was recorded from the ultrasound machine at 10 fps for 120 seconds. Heart rates were measured by palpation before and after the scan, and the average used to estimate heart rate during the scan. Four subjects with collapsed IJVs, as determined by an expert, were excluded from the study. The *Spokes Ellipse* algorithm (described in the next chapter) was applied to all frames collected from each of the 38 remaining subjects, and the first 500 continuously tracked frames were used in subsequent analysis as described below.

5.3. *Automatic Initialization*

The Spokes Ellipse algorithm depends on an initial seed point within each of the vessels it tracks. We explored three methods for initial identification of the blood vessels in the first frame. We describe them here comparing their relative advantages and disadvantages.

5.3.1. Manual Initialization by an Expert

An expert can manually initialize the *Spokes Ellipse* Algorithm by tapping the CCA and IJV on the screen to mark the approximate center of these two vessels. This is inherently a reliable process, given the relative ease with which most experts can identify large vessels in an ultrasound image. In the clinical setting, however, it is desirable not to require such a manual process, especially since it might have to be repeated each time tracking is lost.

5.3.2. Automatic Initialization with Color Doppler

Color Doppler, which detects blood flow, can be used to automatically initialize the ellipses. Although, as outlined above, color Doppler may not reliably differentiate artery from vein when the transducer is perpendicular to the vessels, it does however provide evidence of flow magnitude and can deliver fairly reliable seed points for further determination of artery vs. vein.

To use color Doppler, the ultrasound machine can capture several frames of color Doppler images, which are then thresholded for the existence of significant color (either red or blue). After using the erosion and dilation operators of mathematical morphology to remove noise and outliers, compact clusters of colored pixels that represented the blood vessels can be segmented using connected component analysis. Since there are no other vessels larger than the CCA and IJV in the neck region, the centers of the two largest components are taken to be our putative seed points.

In our implementation of this algorithm we found that the colored pixels within a vessel are not necessarily connected to each other due to turbulence in blood flow, and a nearby smaller vessel can shows up as larger than the fragmented clusters in the larger vessel. In addition, due to the proximity between the CCA and IJV, they can show up on color Doppler as one large cluster instead of two. Thus, we found color Doppler to be unreliable at producing seed points.

5.3.3. Brute Force Testing of each Pixel as a Seed Point

The third option we explored to seed the tracking algorithm is a brute force approach in which the entire image is blanketed with ellipse seed points, and each ellipse then grows according to the *Spokes Ellipse* algorithm. Ellipses that do not fit properly are eliminated until only two properly fitting adjacent ellipses remain. Properly fitting is defined by the criteria listed in Section 5.5. This initialization method proved very reliable and independent of transducer angle. It is especially effective at automatic seeding of the CCA and IJV in this area of the neck (just above the clavicle), since there are rarely other ambiguous structures to confuse it. Therefore we selected this third method of brute force testing, and the reader may assume it was used in all experiments described henceforth in this dissertation.

5.4. Boundary Detection

The boundary at which the spokes in the *Spokes Ellipse* algorithm stops growing is determined by an adaptive binary threshold. A typical ultrasound machine has 8 sliders that control the brightness, or gain, at 8 equally spaced depths. That is, the absolute brightness at different depths does not simply depend on the underlying anatomy or tissue type. A given tissue scanned under different gain settings may produce images that look very different. A monotonic relationship between the intensities of different tissue types should exist that is somewhat linear over a usable range. Therefore, we may be able to find an appropriate binary threshold that separates vessel walls from vessel lumens for each depth level that is simply a certain percentile of the pixel intensities at that depth (or pixel row) in a given image.

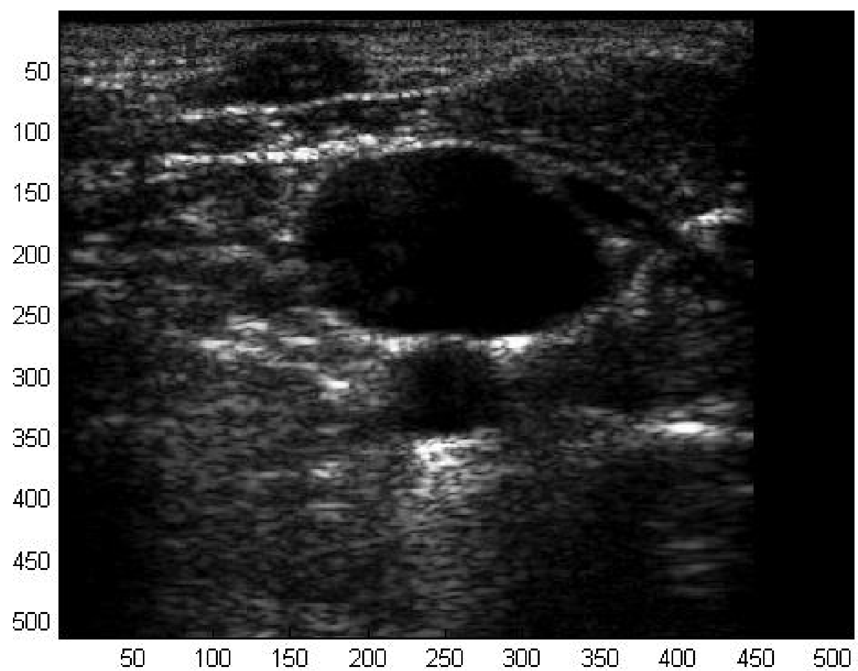

Figure 9. CCA and IJV ultrasound image before adaptive binary thresholding

We experimented with various percentiles as row intensity thresholds on 42 ultrasound images (one from each of our 42 subjects). By visual inspection, the 80th percentile intensity appeared to best define vascular boundaries for both the CCA and IJV. Figure 9 shows an ultrasound image of the CCA and IJV from a particular subject.

Figure 10 shows the corresponding image after applying the adaptive binary thresholding described here using the 80%-tile row intensity. Those pixels whose intensities are above the threshold are considered boundary pixels along a given spoke. Noise will cause false triggering, but the effects should be minimal as long as sufficient number of spokes find the correct boundary.

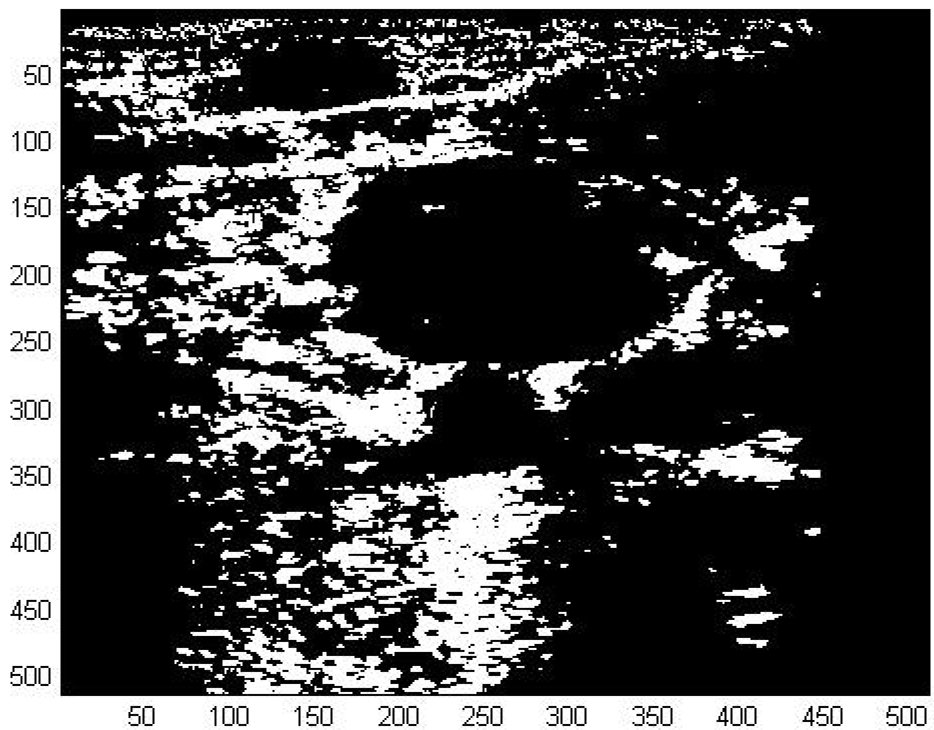

Figure 10. CCA and IJV ultrasound image after adaptive binary thresholding

5.5. Failure Detection

An expert verified that the algorithm successfully tracked the vessels in the first 500 frames for each of 38 subjects. As already mentioned, the other 4 subjects had collapsed veins and their data were consequently excluded. Figure 11 shows an image from one of the 4 subjects, with the IJV clearly containing no patent lumen. The 500 frames from each of the remaining 38 subjects were used to calculate the vessel features. Loss of tracking occurred in several subjects after their first 500 frames. Two of these are shown in Figures 12 and 13. Figure 12 shows loss of tracking resulting from mistakenly eliminating spokes that correctly ended at the vessel wall but are considered to be too long. Figure 13 shows loss of tracking resulting from fitting an ellipse to the CCA when the vascular boundary is incomplete.

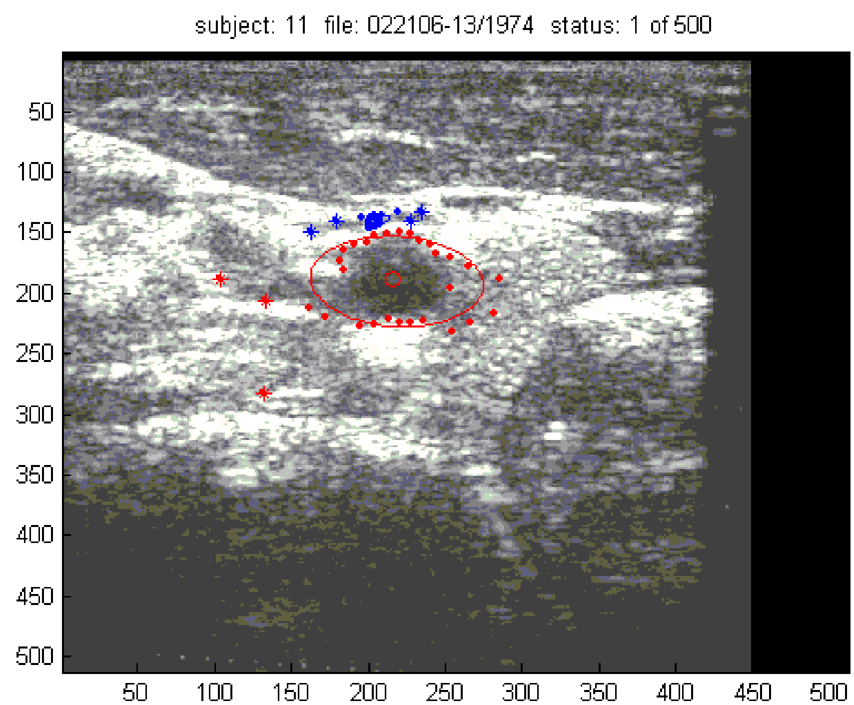

Figure 11. Subject with collapsed vein (upper ellipse with blue dots). Note the algorithm is barely fitting an ellipse to the IJV

While loss of tracking is inevitable, it may not pose an insurmountable problem in a clinical system if it can be detected and corrected by reseeding. Fortunately, there are consistent features we can use to detect loss of tracking. The frames during which tracking was lost each had at least one of the following characteristics generally not seen in frames with properly tracked vessels: (1) ellipse fitting error greater than 0.07, (2) ellipse area less than 5 mm^2, (3) number of spokes finding boundaries less than 10, and (4) the two ellipses separated by more than 0.1 mm. While these results are anecdotal, they indicate that a more extensive study would eventually lead to a reliable system for failure detection and automated reseeding.

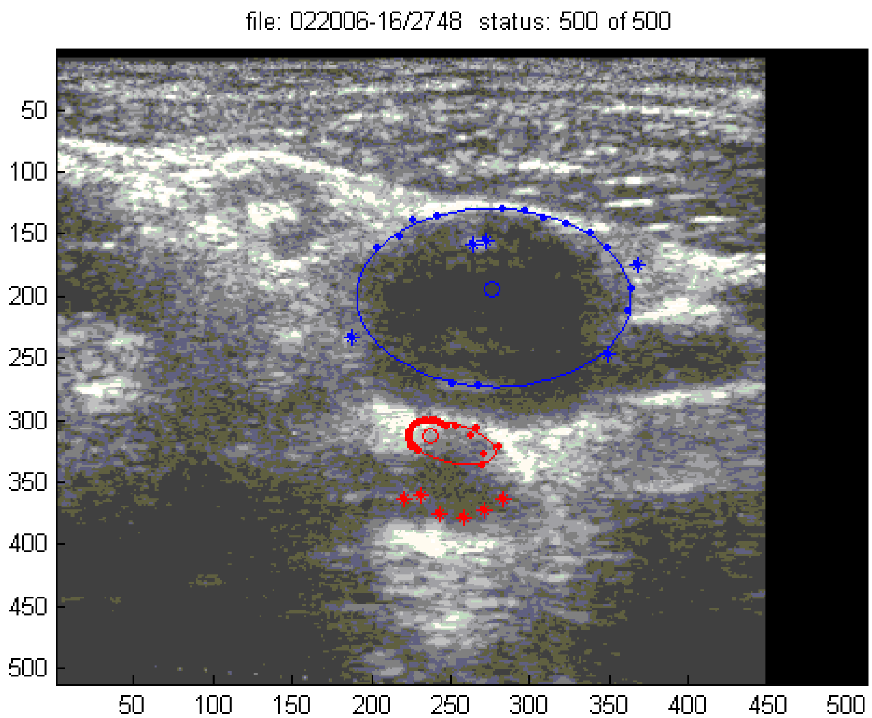

Figure 12. CCA (lower ellipse) with many more short spokes than long spokes, resulting in a loss of tracking for the CCA. Some of the CCA spokes are mistakenly considered to be too long and consequently excluded from the ellipse fitting.

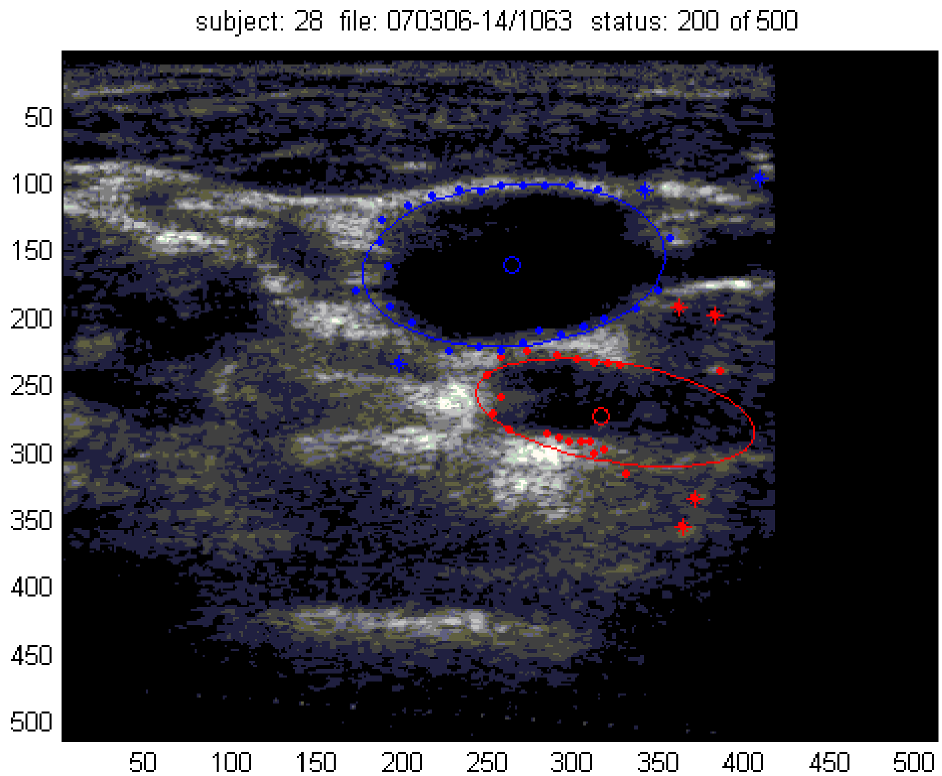

Figure 13. CCA (lower ellipse) with incomplete border on ultrasound, resulting in a fitted ellipse that "leaked" out of the walls of the CCA.

5.6. Validation

The *Spokes Ellipse* algorithm is based on two assumptions: (1) the vessels' cross sections are elliptical, and (2) the algorithm-drawn ellipses are similar to ellipses fit to manual traces of the lumen drawn by an expert. We define the percent similarity between two areas as

$$\frac{2 \times (Area\ 1 \cap Area\ 2)}{Area\ 1 + Area\ 2} \times 100 \qquad (1)$$

using the Dice Similarity Metric [37]. A perfect similarity between two areas would thus have a value of 100% while two areas that do not overlap at all would deliver a similarity of 0%.

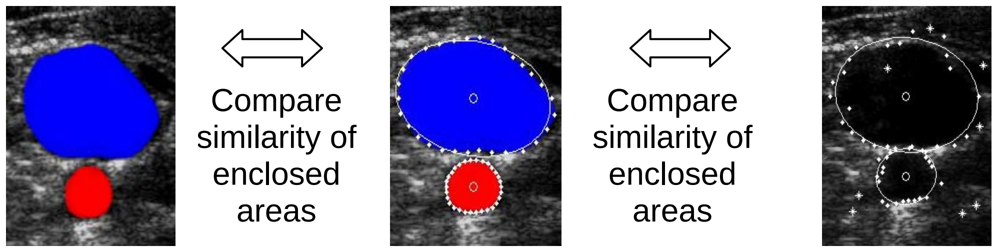

A. Expert tracing B. Ellipses fit to expert tracing C. *Spokes Ellipse* Algorithm applied to original image

Figure 14. Similarity between the area of an ellipse (B) fit to the expert tracing and the expert tracing itself (A) as well as the ellipse found directly on the image data by the Spokes Ellipse Algorithm (C).

An expert segmented 5 random image frames per subject. We compared the manual segmentations against those derived from the *Spokes Ellipse* algorithm (Figure 14) in two steps, by comparing the area of the ellipse fit to the expert tracing and (1) the expert traced area itself, and (2) the algorithm defined ellipse, to test assumptions 1 and 2, respectively.

Table 3. Similarity between vessel cross-sectional area estimations (95% confidence interval)

	Segmented vessel versus ellipse fit to segmented vessel	Ellipse fit to segmented vessel versus ellipse fit to unsegmented vessel
CCA	96.8 ± 1.2%	84.5 ± 7.0%
IJV	93.8 ± 3.1%	89.6 ± 6.1%

As shown in Table 3, for the 190 sampled images (38 subjects x 5 random frames from each), there was a high similarity between the manual tracings of the lumen and the ellipses fitted to those tracings, indicating that the cross-sectional areas of the vessels were reasonably elliptical (assumption 1). The high similarity between ellipses fit to the manual tracings and ellipses fit directly to the image data by the *spokes-ellipse* algorithm indicates that the algorithm had basically extracted the same elliptical shape as the expert (assumption 2).

Chapter 6. Calculation of Vessel Features

Having validated the *Spokes Ellipse* algorithm for basic segmentation, we next tested its use in generating features for vessel classification. For each subject, cross-sectional areas of the CCA and IJV were calculated by applying the Spokes Ellipse algorithm to each of the 500 frames and the Fourier transform applied to the area as a function of time. This allowed for determination of the heart rate and respiratory rate, as well as magnitude and phase as a function of frequency. In particular, the phase at the heart rate for both the CCA and IJV was found to be consistent enough to reliably calculate phase differences between the vessels, as will be described below.

6.1. Number of Eligible Spokes

Each ultrasound frame analyzed by the *Spokes Ellipse* algorithm is assumed to arrive with a seed point, either from the initialization procedure described above for the first frame in a series, or from the center of the ellipse fit to the previous frame. From each seed point, the *Spokes Ellipse* algorithm grows 30 evenly spaced spokes until they reach the thresholded boundary intensity or some predetermined maximum length. However, due to speckle, some spokes incorrectly stopped growing within vessels and were thus too short. Alternatively, because of incomplete vessel borders, some spokes grew past vessel boundaries and were too long. Our preliminary study showed that keeping only the spokes whose length were within one standard deviation of the mean produced a population that terminated reliably near the vascular wall. We recorded the number of such spokes determined to be eligible for every frame.

6.2. Ellipse Area

Given a set of endpoints from the eligible spokes, the ellipse fitting algorithm returned the parameters of the ellipse including the center point location and the radii and orientations of major and minor axes. The ellipse area was calculated by multiplying the product of the major and minor axes by π.

6.3. Ellipse Fitting Error

In fitting an ellipse to the eligible spokes, some error was inevitable. The fitting error was calculated by taking the root-mean-square difference between the eligible spokes' endpoints and the fitted ellipse.

6.4. Vessel Depth

We examined whether the IJV is consistently closer to the skin than the CCA as well as their absolute depths (measured by distance between the centers of each vessel to the skin).

6.5. Eccentricity

Because arteries have a thicker muscular layer that can withstand higher pressure than veins, they are stiffer and would seem more likely to be circular. Veins are more compliant and contain blood at a lower pressure, so they would seem less likely to assume a circular shape. We calculated eccentricity of the ellipse, defined as:

$$eccentricity = \sqrt{1 - \frac{b^2}{a^2}} \quad (2)$$

where *a* is the radius of the semi-major axis and *b* is the radius of the semi-minor axis.

6.6. Heart Rate and Respiratory Rate

By taking the Fourier transform of the temporal series of cross sectional areas for each vessel, we can obtain a magnitude and phase at each frequency. The heart rate was determined by identifying the frequency with the greatest magnitude between 40 and 150 cycles per minute (cpm). Similarly, the respiratory rate was determined as the frequency with greatest magnitude in the range 10 to 30 cpm.

6.7. Compliance Measure

As already mentioned, an artery generally has a thicker muscular layer than a similar sized vein. Thus the artery is stiffer while the vein is more compliant. A stiffer material emphasizes high frequencies and attenuates low frequencies. A compliant material does the opposite. Thus we may expect differences in the spectral content of wall motion between the CCA and the IJV. We analyzed this phenomenon by calculating the slope of the linear regression that best fit the magnitude of the Fourier transform from 10-250 cpm.

6.8. Phase Differences

Recall that the Fourier transform $X(\omega)$ of a signal $x(t)$ can be represented in phasor notation as

$$X(\omega) = r(\omega)e^{j\theta(\omega)} \tag{3}$$

where $r(\omega) \geq 0$ is the magnitude and $-\pi < \theta(\omega) \leq \pi$ is the phase in the complex plane. Denoting the Fourier transforms of the IJV and CCA cross-sectional areas respectively as $J(\omega)$ and $C(\omega)$, the phase difference $Q(\omega)$ between the CCA and IJV can be found from their ratio, normalized by their relative magnitudes,

$$Q(\omega) = \frac{r_J(\omega)}{r_C(\omega)} \frac{C(\omega)}{J(\omega)} = e^{j(\theta_C(\omega) - \theta_J(\omega))}. \tag{4}$$

This yields a unit phasor, the phase of which is the difference between the phases of the CCA and IJV at frequency ω,

$$\Delta\theta(\omega) = \theta_C(\omega) - \theta_J(\omega). \tag{5}$$

Thus,

$$\Delta\theta(\omega) = \arctan \frac{\mathrm{Im}\{Q(\omega)\}}{\mathrm{Re}\{Q(\omega)\}} \tag{6}$$

Since we have a sampled Fourier transform, individual phase samples may or may not represent a consistent phase difference, so we convolve over a narrow band in the frequency domain with a normalized Gaussian smoothing filter $G(\omega,\sigma)$ as follows

$$\Delta\tilde{\theta}(\omega) = \arctan\frac{\mathrm{Im}\{G(\omega,\sigma) * Q(\omega)\}}{\mathrm{Re}\{G(\omega,\sigma) * Q(\omega)\}}, \quad (7)$$

with σ set empirically to 3 samples or 2.5 cpm in the Fourier frequency domain. (Note that convolution can be applied to the complex number $Q(\omega)$ by applying it independently to the real and imaginary parts).

6.9. Phase Consistency

A measure of phase consistency for this smoothed phase difference is

$$\alpha(\omega) = \left|G(\omega,\sigma) * Q(\omega)\right|. \quad (8)$$

Random phase differences in individual samples of the Fourier transform due to noise tend to cancel upon convolution with the Gaussian, yielding a value of $\alpha(\omega)$ near 0, whereas a consistent phase shift over consecutive frequency samples of the Fourier transform yields a value of $\alpha(\omega)$ near 1, since the area under normalized Gaussian is 1.

Chapter 7. Vessel Features from the Training Set

In this chapter, we review the results from extracting each the features defined above from our training set of 500 consecutive images from each of 38 ultrasound subjects.

7.1. Number of Eligible Spokes

The number of eligible spokes among the total of 30 initiated on each vessel by the *Spokes Ellipse* algorithm serves as a measure of how well the vessel was detected. Recall that spokes are eliminated from being more than one standard deviation either longer or shorter than the mean length for that given vessel and frame. Short spokes commonly result from specular noise within vessels. Since similar noise levels were observed throughout a given sequence of ultrasound images, we should expect similar numbers of spokes judged too short for each vessel in each image. The spokes judged as too long would then account for the difference in the number of eligible spokes for each subject. They are a direct reflection of the completeness of the vascular boundaries, since it is spokes that grow beyond a boundary gap that are eliminated as being too long. The data in Table 4 show that the CCA produced fewer usable spokes than the IJV, and that this difference is significant. This means the boundary of the CCA is more likely to be ill-defined than the IJV. A direct consequence is that the ellipse fitting error is also greater when fitting ellipses to the CCA compared to the IJV, as will be described in section 8.3.

Table 4. Number of eligible spokes for each subject

	Vessel	95% Confidence Interval	P-value
Mean	CCA	23.24 ± 0.55	0.000
	IJV	24.26 ± 0.38	
Standard deviation	CCA	1.61 ± 0.09	0.006
	IJV	1.44 ± 0.08	
Lower 10th percentile	CCA	21.24 ± 0.58	0.000
	IJV	22.39 ± 0.38	
Upper 90th percentile	CCA	25.18 ± 0.54	0.002
	IJV	26.00 ± 0.44	

*The last column shows the significance level (*p*) for a paired t-test comparing the CCA and IJV values across the subjects.

7.2. Ellipse Area

Given our calculations of area from the ellipses fit to the CCA and IJV on each ultrasound frame, we compared these areas over the population of 38 subjects. Since the blood volume is more dependent on gravity in the vein than in the artery, having the subject lie supine increased the blood volume in the IJV significantly (Table 5), resulting in ellipse cross sectional areas of the IJV that were larger than those of the CCA. Figure 15 shows a comparison between the temporal series of the CCA and IJV cross-sectional areas for a typical subject.

Table 5. Ellipse areas (mm^2) for each subject

	Vessel	95% Confidence Interval	P-value
Mean	CCA	20.56 ± 1.49 mm^2	0.000
	IJV	39.87 ± 6.28 mm^2	
Standard deviation	CCA	2.985 ± 0.521 mm^2	0.001
	IJV	4.197 ± 0.615 mm^2	
Lower 10th percentile	CCA	17.15 ± 1.38 mm^2	0.000
	IJV	34.54 ± 5.95 mm^2	
Upper 90th percentile	CCA	24.42 ± 1.91 mm^2	0.000
	IJV	45.11 ± 6.66 mm^2	

*The last column shows the significance level (*p*) for a paired t-test comparing the CCA and IJV values across the subjects.

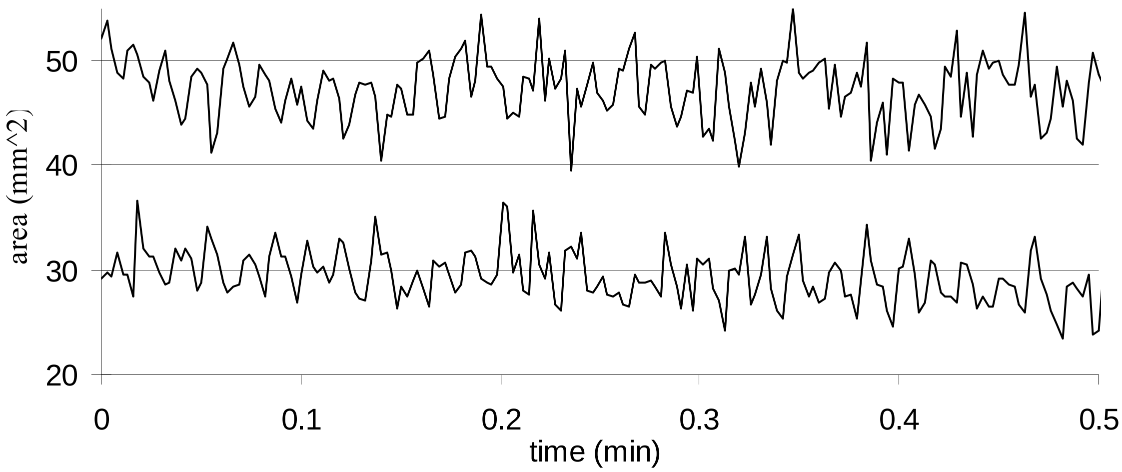

Figure 15. Time series of the cross sectional areas of the IJV (top) and the CCA (bottom) in a typical subject (subject #33) in 30 seconds. Note the peaks and troughs are generally out of phase.

7.3. *Ellipse Fitting Error*

As already mentioned in Section 8.1, the CCA tends to have fewer eligible spokes than the IJV, because its boundaries are less well defined. Therefore, the CCA has a higher ellipse fitting error (0.0247 ± 0.0030 vs 0.0146 ± 0.0020 for the IJV, see Table 6).

Table 6. Ellipse Fitting Error for each subject

	Vessel	95% Confidence Interval	P-value
Mean	CCA	0.0247 ± 0.0030	0.000
	IJV	0.0146 ± 0.0020	
Standard deviation	CCA	0.0101 ± 0.0012	0.000
	IJV	0.0068 ± 0.0010	
Lower 10th percentile	CCA	0.0134 ± 0.0017	0.000
	IJV	0.0077 ± 0.0013	
Upper 90th percentile	CCA	0.0385 ± 0.0047	0.000
	IJV	0.0234 ± 0.0033	

*The last column shows the significance level (p) for a paired t-test comparing the CCA and IJV values across the subjects.

7.4. Vessel Depth

Vessel depth has been discussed as a distinguishing feature between the CCA and the IJV. Table 7 shows that the CCA generally lies deeper than the IJV. This may help explain the degradation in its boundaries since the ultrasound suffers more attenuation in reaching deeper tissue. The use of this difference, however, raises some complex issues involving clinical protocols, which will be discussed further in a later section.

Table 7. Vessel Depth (mm) for each subject

	Vessel	95% Confidence Interval	P-value
Mean	CCA	2.364 ± 0.126 mm	0.000
	IJV	1.583 ± 0.079 mm	
Standard deviation	CCA	0.0519 ± 0.0072 mm	0.000
	IJV	0.0336 ± 0.0059 mm	
Lower 10th percentile	CCA	2.302 ± 0.124 mm	0.000
	IJV	1.545 ± 0.078 mm	
Upper 90th percentile	CCA	2.431 ± 0.128 mm	0.000
	IJV	1.625 ± 0.081 mm	

*The last column shows the significance level (*p*) for a paired t-test comparing the CCA and IJV values across the subjects.

7.5. Eccentricity

It was expected that, being more compliant, the IJV would show a greater degree of eccentricity, especially considering the pressure being applied by the ultrasound transducer, which is often observed to cause further compression of the vein. The application of such pressure, in fact, is often used clinically to differentiate arteries from veins in general. However, the respective means of eccentricity for the CCA and IJV were 0.66 ± 0.03 and 0.68 ± 0.02 (Table 8), a non-significant difference, indicating that the eccentricity of the vessels is not a good distinguishing feature. Eccentricity is inherently dependent on the angle between image plane and direction of the vessel, so that even circular vessels can appear eccentric when scanned at an angle. The slightly higher standard deviation of eccentricity for the CCA also conflicts with the expectation that the IJV would show a greater variation in eccentricity over time, and as such is suspect as a reliable differentiating factor, despite its statistical significance.

Table 8. Eccentricity for each subject

	Vessel	95% Confidence Interval	P-value
Mean	CCA	0.66 ± 0.03	0.144
	IJV	0.68 ± 0.02	
Standard deviation	CCA	0.09 ± 0.01	0.000
	IJV	0.06 ± 0.01	
Lower 10^{th} percentile	CCA	0.54 ± 0.03	0.010
	IJV	0.60 ± 0.03	
Upper 90^{th} percentile	CCA	0.76 ± 0.02	0.333
	IJV	0.76 ± 0.02	

*The last column shows the significance level (*p*) for a paired t-test comparing the CCA and IJV values across the subjects.

7.6. Heart Rate and Respiratory Rate

The heart rate and respiratory rate would not be expected to differ between the CCA and IJV, but these measures were examined in part to establish their reliability, especially since we hoped to determine the phase difference of the pulses in the two vessels at the heart rate. The functions of cross sectional area vs. time of the CCA and IJV in a typical subject are shown in Figure 15, and their Fourier transforms are shown in Figure 17a and b. The heart rate in this subject corresponds to the peak in magnitude around 60 cpm and is consistent with that determined by palpation during the scan. Although the heart rates extracted from the transform for each vessel should theoretically be identical, according to Table 9, the p-value (<0.05) indicates there is a reliable difference. But this difference is small, with the 95% confidence intervals overlapping substantially. According to Figure 16, the heart rate from CCA is usually the same as that from the IJV. When the heart rates are not the same, the heart rate tends be smaller when coming from the CCA. One would not expect it to be a significant discriminator, and yet when combined with 4 other features, it turned out to be one of the top 5 features that can be used to reliably discriminate between the CCA and IJV, as will be seen in Chapter 9. Clearly, taking the peak magnitude in a sampled Fourier transform must be measuring something more subtle than simple periodicity of an assumed constant heart-rate, which should theoretically be identical for the two vessels.

The respiratory rates extracted from the two Fourier transforms did not differ significantly. Therefore, as expected, this measure is not useful for distinguishing between the two vessels.

Table 9. Heart Rates and Respiratory Rates for each subject

	Vessel	95% Confidence Interval	P-value
Heart rate (cpm)	CCA	61.08 ± 2.55	0.018
	IJV	62.69 ± 2.39	
Magnitude at heart rate	CCA	20624 ± 2968	0.000
	IJV	43579 ± 7983	
Respiratory rate (cpm)	CCA	16.47 ± 1.36	0.054
	IJV	18.09 ± 1.17	
Magnitude at respiratory rate	CCA	16857 ± 2660	0.000
	IJV	27502 ± 4502	
Slope of best fit line between 10 – 250 cpm	CCA	-15.49 ± 2.37	0.000
	IJV	-35.50 ± 6.16	

*The last column shows the significance level (*p*) for a paired t-test comparing the CCA and IJV values across the subjects.

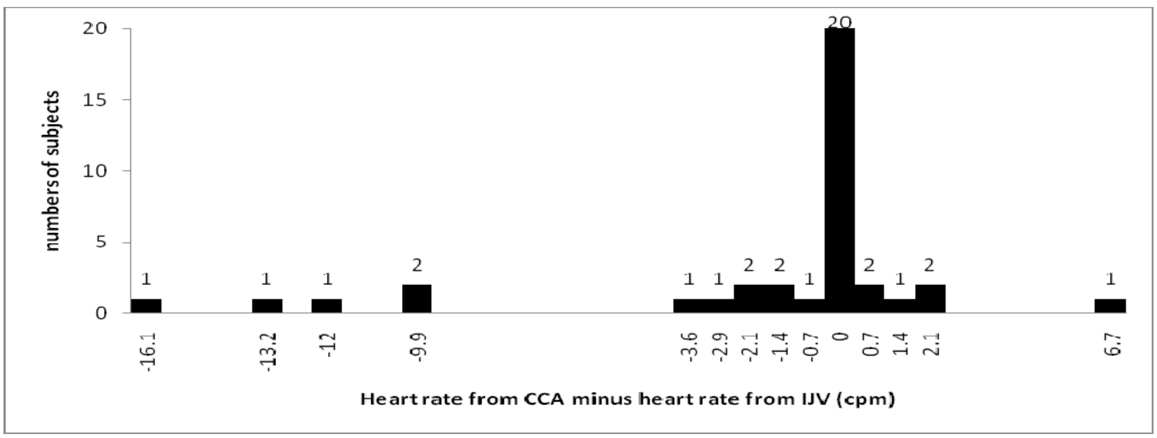

Figure 16. Ratio of CCA heart rate to IJV heart rate on a per subject basis

7.7. *Compliance Measure*

The slope of the magnitude in the Fourier transform of the IJV (-35.50 ± 6.16) as determined by linear regression over the frequencies (10 – 250 cpm), is significantly more negative than that of the CCA (-15.49 ± 2.37), with a p-value < 0.05. This is consistent with the IJV being more compliant than the CCA and thus attenuating the higher frequencies to a larger extent. This also may in part explain the higher magnitude of the IJV Fourier transform at the heart rate and respiratory rate, which are typically in the lower half (10 – 130 cpm) of the spectrum.

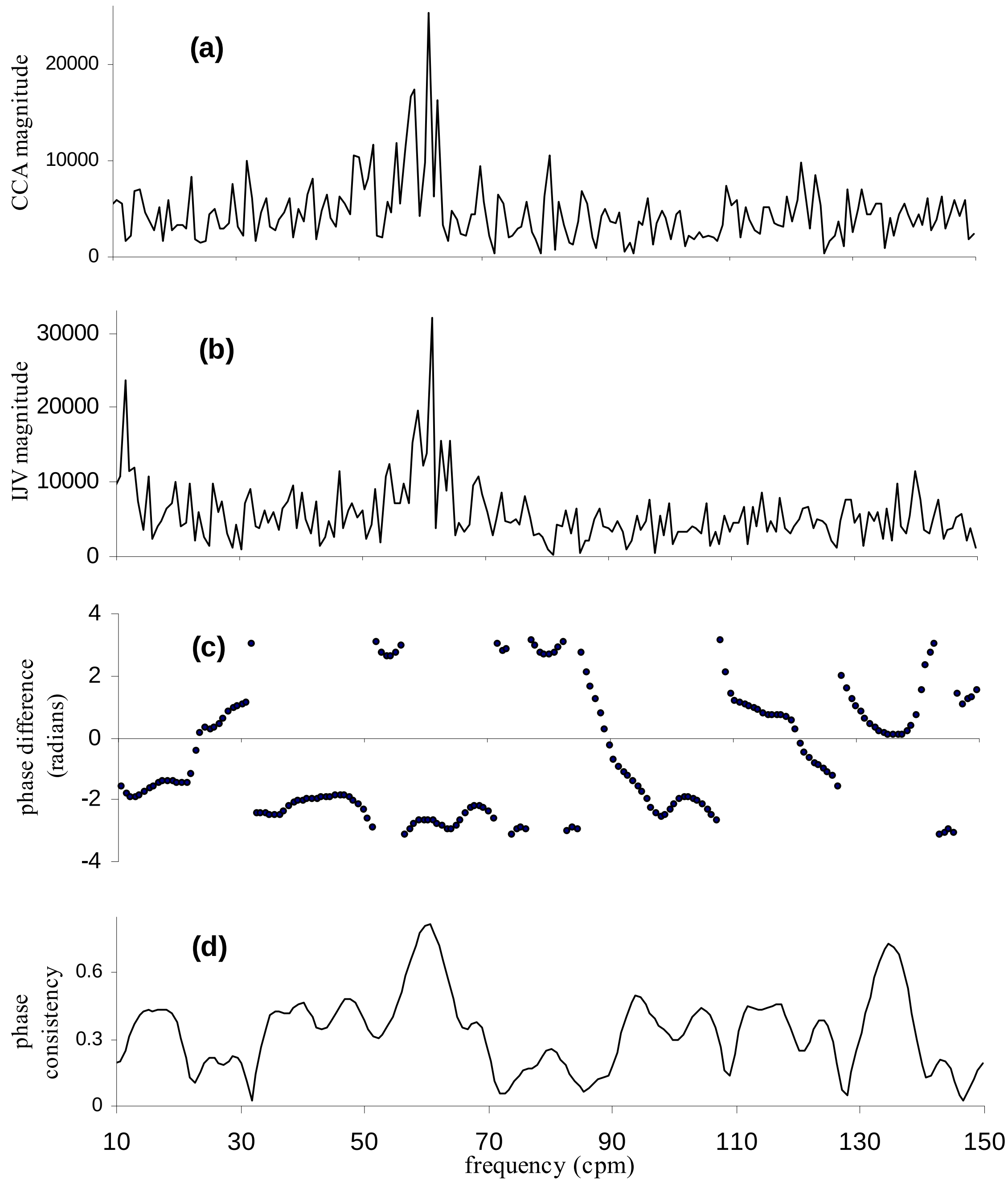

Figure 17. Parameters in the frequency domain 10-150 cpm for subject #33: (a) Magnitude of the Fourier transform of the time series of CCA cross sectional areas. (b) Magnitude of the Fourier transform of the time series of IJV cross sectional areas. (c) Phase difference between CCA and IJV as a function of frequency. (d) Phase consistency between CCA and IJV as a function of frequency.

7.8. Phase Differences

The phase difference between the CCA and IJV as a function of frequency is unique among the characteristics that we studied in that it wraps around from $-\pi$ to π. We are particularly interested in the phase difference at the heart rate, since it is here that we expect one vessel to consistently lead the other. Indeed, phase difference at the heart rate was measured to have a 95% confidence interval of -1.65 ± 0.54 radians. If we had reversed the CCA and IJV in the calculation of phase difference, the 95% confidence interval would simply be the negative, i.e., 1.65 ± 0.54 radians. Since these confidence intervals include neither 0 nor π, it appears that phase difference can be reliably used to differentiate between the CCA and the IJV. For the particular patient shown in Figure 17 near the heart rate of 60 cpm, the phase difference is 2.2 radians.

7.9. Phase Consistency

Phase differences show high consistencies (0.61 ± 0.05) around the frequency of the heart rate. The subject in Figure 17, for example, shows a phase consistency (Figure 17d) that peaked as high as 0.9 at the frequency of the heart rate. This reaffirms our confidence in our method of measuring phase difference as well as our determination in the reliability of the underlying parameter for classifying the vessels relative to each other.

Chapter 8. Vessel Classifications

In the previous chapter, we reviewed individual characteristics or features as candidates for differentiating between the CCA and the IJV. In this chapter, we describe a classification scheme for the two vessels, based on an optimal combination of those individual features.

The vessel classification problem can be reduced to ordering the elements of a set: {CCA, IJV}. Given a pair of vessels with feature vectors ($\mathbf{v_{ki}}$, $\mathbf{v_{(1\text{-}k)i}}$), where k equals 0 or 1, in a series of tracked ultrasound images from a subject *i*, we wish to determine k such that $\mathbf{v_{0i}}$ = CCA and $\mathbf{v_{1i}}$ = IJV. This is equivalent to determining the order in which the vessels were given where {CCA, IJV} is group $k = 0$ and {IJV,CCA} is group $k = 1$.

We represent the *m* characteristics of each vessel for each subject *i* by the *m*-dimensional vectors:

$$\begin{aligned} \mathbf{v_{ki}} &= (v_{ki1}, v_{ki2}, \ldots, v_{kim}) \\ \mathbf{v_{(1\text{-}k)i}} &= (v_{(1\text{-}k)i1}, v_{(1\text{-}k)i2}, \ldots, v_{(1\text{-}k)im}) \end{aligned} \tag{9}$$

The difference **d** is calculated between each pair of vessels for each subject *i*:

$$\begin{aligned} \mathbf{d_{ki}} &= \mathbf{v_{ki}} - \mathbf{v_{(1\text{-}k)i}} \\ \mathbf{d_{(1\text{-}k)i}} &= \mathbf{v_{(1\text{-}k)i}} - \mathbf{v_{ki}} \end{aligned} \tag{10}$$

Note that phase difference is a property between two vessels and not of either vessel alone. It is already in the form of $\mathbf{v_{0i}} - \mathbf{v_{1i}}$ for $\mathbf{d_{0i}}$, so we can simply take the negative to obtain $\mathbf{v_{1i}} - \mathbf{v_{0i}}$ for $\mathbf{d_{1i}}$.

With this representation of the parameters, our goal is to find a set of weights $\mathbf{w} = (w_1, w_2,...,w_m)$ such that $\mathbf{w}\cdot\mathbf{d}_{0i}$ is positive and $\mathbf{w}\cdot\mathbf{d}_{1i}$ is negative. In other words, if $\mathbf{w}\cdot\mathbf{d}_{ki}$ is positive then the first and second given vessels are most likely to be CCA and IJV respectively. If not, then they are most likely to be IJV and CCA respectively instead. The weights can be found through Fisher's linear discriminant analysis (LDA) [38].

If we include the mean, standard deviation, and upper and lower percentiles for each feature, we have a total of 26 parameters for vessel classification. However, such a large feature space (m = 26) may result in over-fitting. In over-fit models, variables which truly do have the power to predict the correct group are somewhat marginalized in their importance, and the predicting power of the "weak" features tends to be greatly over-exaggerated. Therefore, we need to reduce the dimensionality of the feature space. We do this in a systematic way in Section 9.2. But first we eliminate one feature, at least temporarily, in the next section, even though it does in certain circumstance represent a significant discriminating feature.

8.1. Temporary Elimination of Depth as a Feature

Depth is a potentially important feature to distinguish the two vessels since the CCA generally lies deeper beneath the skin than the IJV. However, the relative locations of two vessels in the image depend on how the transducer is oriented and what portion of the neck is being scanned. One study has shown the IJV to be positioned completely lateral to the CCA in 8.7% of clinical scans [39]. Actually, doctors often prefer such lateral placement of the IJV because CCA puncture is less likely when it is not directly under the IJV. This reduces the potential usefulness of depth in vessel identification.

By not considering the depth parameter for now, we reduced the number of parameters for each subject from 26 to 22.

8.2. Step-wise Fisher's Linear Discriminant Analysis with Wilk's Lambda

Twenty-two features is still a very large number of dimensions for a feature space. To identify the set of the most significant parameters among them, we used stepwise linear discriminant analysis (SLDA) as implemented in the statistical package SPSS (Statistical Package for the Social Sciences, Chicago, IL) with Wilks' lambda as the measure of significance. Wilk's Lambda is a negative correlate of a variable's importance: The smaller the Wilks' Lambda, the more important the variable. SLDA works by starting with the null set of variables and adds one variable at a time: the variable which most reduces the Wilks's lambda of the set. The addition of variables continues until no more significant variables can be identified. This reduced the dimensionality of the feature space on which Fisher's LDA subsequently operates to determine **w**. A leave-one-subject-out analysis was performed to validate the SLDA's parameter selection as well as the subsequent Fisher's LDA calculation of **w**.

Table 10. Stepwise Wilks' Lambda statistics and Standardized canonical discriminant function coefficients (wi)

Step	Variable entered at each step	Wilks' Lambda*	w_i
1	Difference in slope of Fourier transform's lower frequency spectrum trendline	0.479	0.674
2	Phase shift between vessels	0.264	-0.755
3	Difference in mean error	0.174	-1.793
4	Difference in heart rate from vessels	0.133	1.067
5	Difference in the upper 90th percentile ellipse fitting error between the vessels	0.126	1.057

* Wilk's Lambda at each step is inversely correlated with the importance of the combined set of variables at that step and all the previous steps.

We used SLDA in SPSS to determine the best predictor variables for this data set (Table 10), further reducing the parameter space from 22 to 5. We then applied Fisher's linear discriminant analysis to these 5 parameters to determine the weights (w_i in Table 10) that best separate the two classes of vessel permutations.

We applied the weights to all data points and calculated the dot product of w_i and d_i. The results are shown in Figure 18. Data points representing class 0 are diamond shaped while those representing class 1 are circles. We then applied leave-one-subject-out analyses in which one subject was used for testing while the remaining 37 subjects were used for training. These results are represented by +'s for class 0 and x's for the class 1. The two permutation classes are separated completely by the zero-line and are mirror images of each other, a consequence of their underlying parameters being negatives of each other. They also appear to cluster around 0.26 and -0.26 respectively. The leave-one-subject-out studies show a greater degree of variance from the cluster centroids, but they are still separated completely by the zero-line.

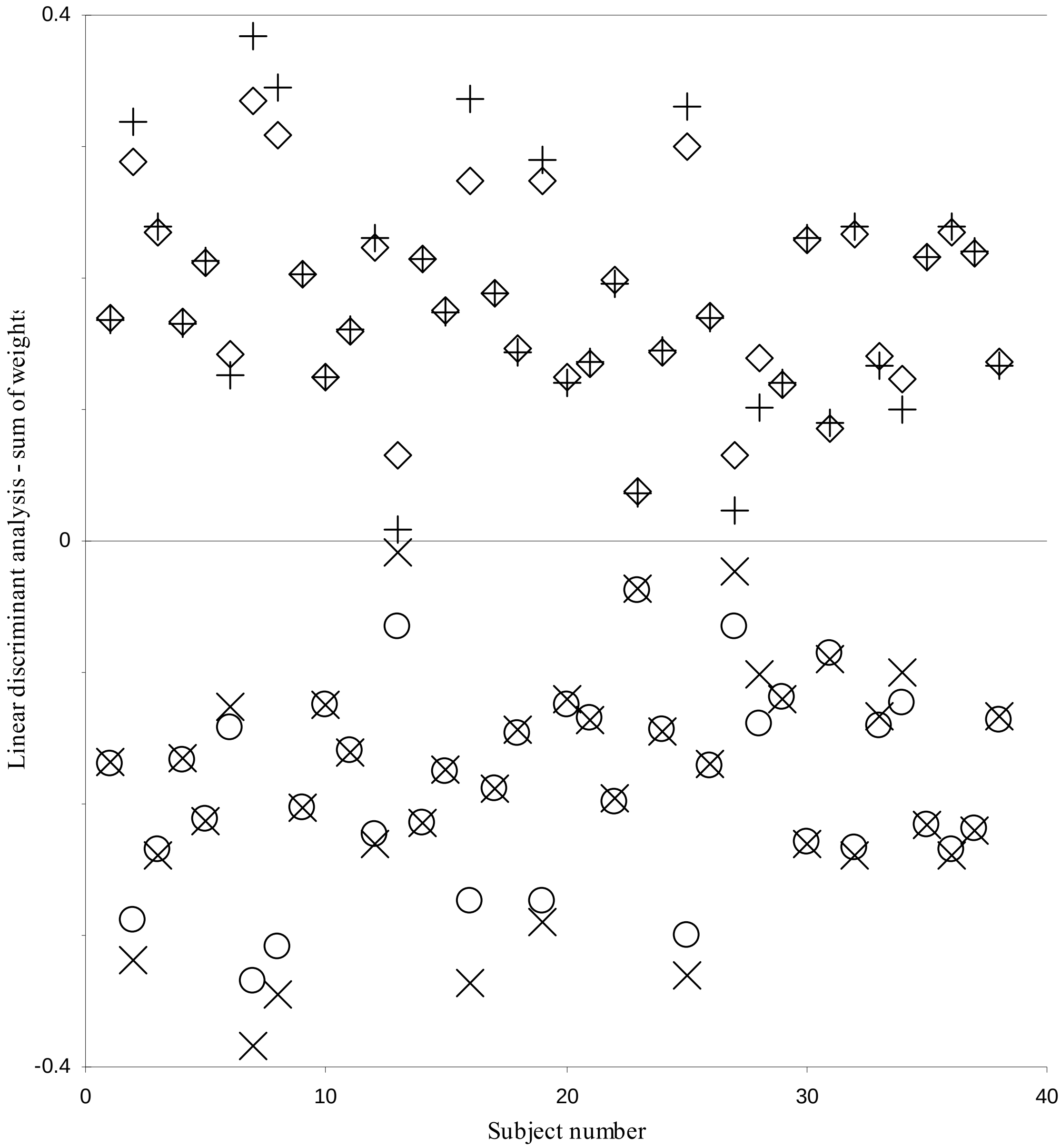

Figure 18. Fisher's linear discriminant analysis applied to all 38 subjects. Diamonds represent the permutation {CCA, IJV} whose parameters are weighed and summed based on weights derived from the entire 38-subject training set. Circles represent the other permutation: {IJV, CCA}. +'s represent the permutation {CCA, IJV} from each subject whose parameters are weighed and summed based on weights derived from the other 37 subjects. X's represent the other permutation.

A histogram (Figure 19) shows the same data in a different format, clearly demonstrating that the linear discriminant analysis of the 5 parameters separates the two permutation classes into two well-defined, approximately normally distributed, mirror-image clusters in leave-one-out studies. The dot products for all the CCA/IJV permutations are above 0 while the IJV/CCA permutations are below 0.

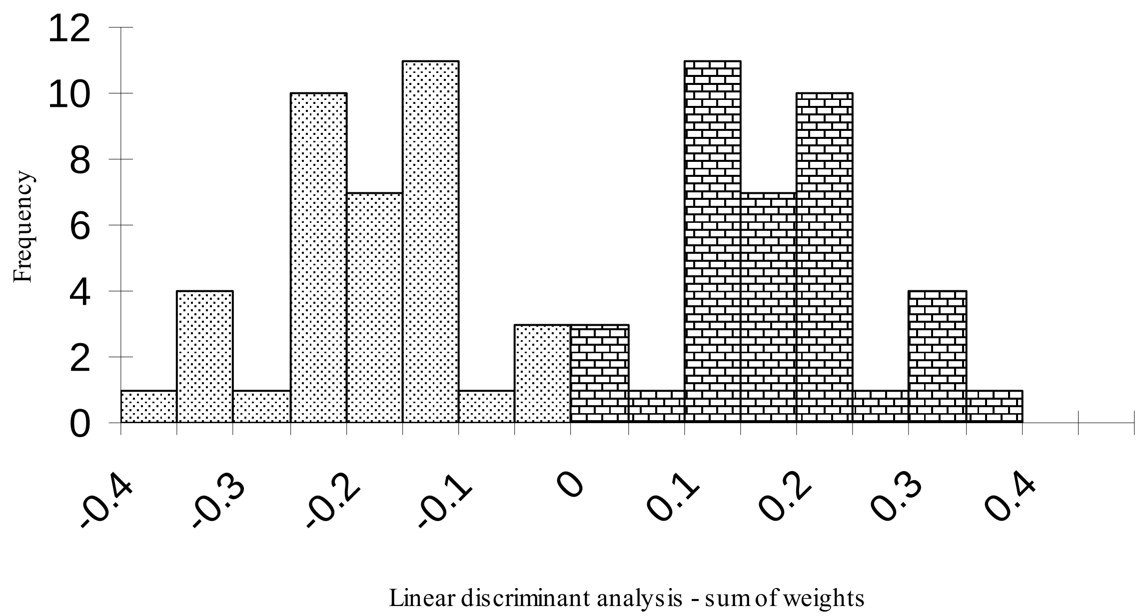

Figure 19. Frequency distribution of the weighted sum of the parameters on each subject using weights derived from Fisher's linear discriminant analysis of the other 37 subjects. The dotted histograms represent the {IJV, CCA} permutations while the brick textured histograms represent the {CCA, IJV} permutations.

The results on these data demonstrate that our method automatically and accurately distinguishes between the CCA and IJV in B-mode ultrasound.

Chapter 9. Conclusion

We have shown in each of our 38 subjects (after excluding 4 with collapsed IJVs) that the spokes ellipse algorithm maintained tracking for at least 50 seconds (500 continuous frames) during the 120 second ultrasound scans. We have also identified criteria for detecting loss of tracking, which can be used to prompt reinitialization. Although the CCA and IJV both pulsate, we have verified that the differences in depth of the vessels alone can distinguish between the vessels, at least at the position in the neck that we used in this experiment. However, in clinical situations doctors often seek probe positions that orient the vessels side by side. A combination of other intrinsic vessel properties can be used to distinguish reliably between the vessels: the slopes of the Fourier transforms, phase shift between the vessels, heart rate as determined from the Fourier transforms, and the mean and upper 90th percentile ellipse fitting error. The only truly surprising member of this set of top 5 features is heart rate as determined from the Fourier transform. As already mentioned, taking the peak magnitude in a sampled Fourier transform can measure something beyond simple periodicity, perhaps due to the fact that the heart-rate is not truly constant, or perhaps due to some more subtle interaction between the transform and the differing harmonic structure of the two vessels.

9.1. Real-Time Implementation

Based on these off-line studies with training data, a real-time system has been constructed into a clinical ultrasound machine that examines the image frames (Figure 20), determines the locations of two candidate vessels by brute force ellipse fitting (Figure 21), fits ellipses using the *Spokes Ellipse* algorithm, calculates the chosen top 5 features, and applies the LDA analysis. In just a few seconds, after sufficient frames have been acquired to perform a Fourier transform, the system marks the CCA red and the IJV blue, (or in the indeterminate case, as described below in Section 10.2, both are marked green) as shown in Figure 22. These graphically overlaid markers are projected within the patient along with the ultrasound image by the Sonic Flashlight. After initialization, the system tracks in real-time by using a sliding window of previous frames. Our preliminary results on healthy subjects in their 20s show that the system reliably detects and labels the CCA and IJV in almost all cases.

When loss of tracking occurs, we first assume the previous frame is correct and reuse the same seed points. This reseeding is much faster than applying the brute force initialization, which can take between 5 to 10 seconds to converge. When 10 consecutive frames are considered lost, the algorithm terminates to alert the operator that significant changes have occurred in the images.

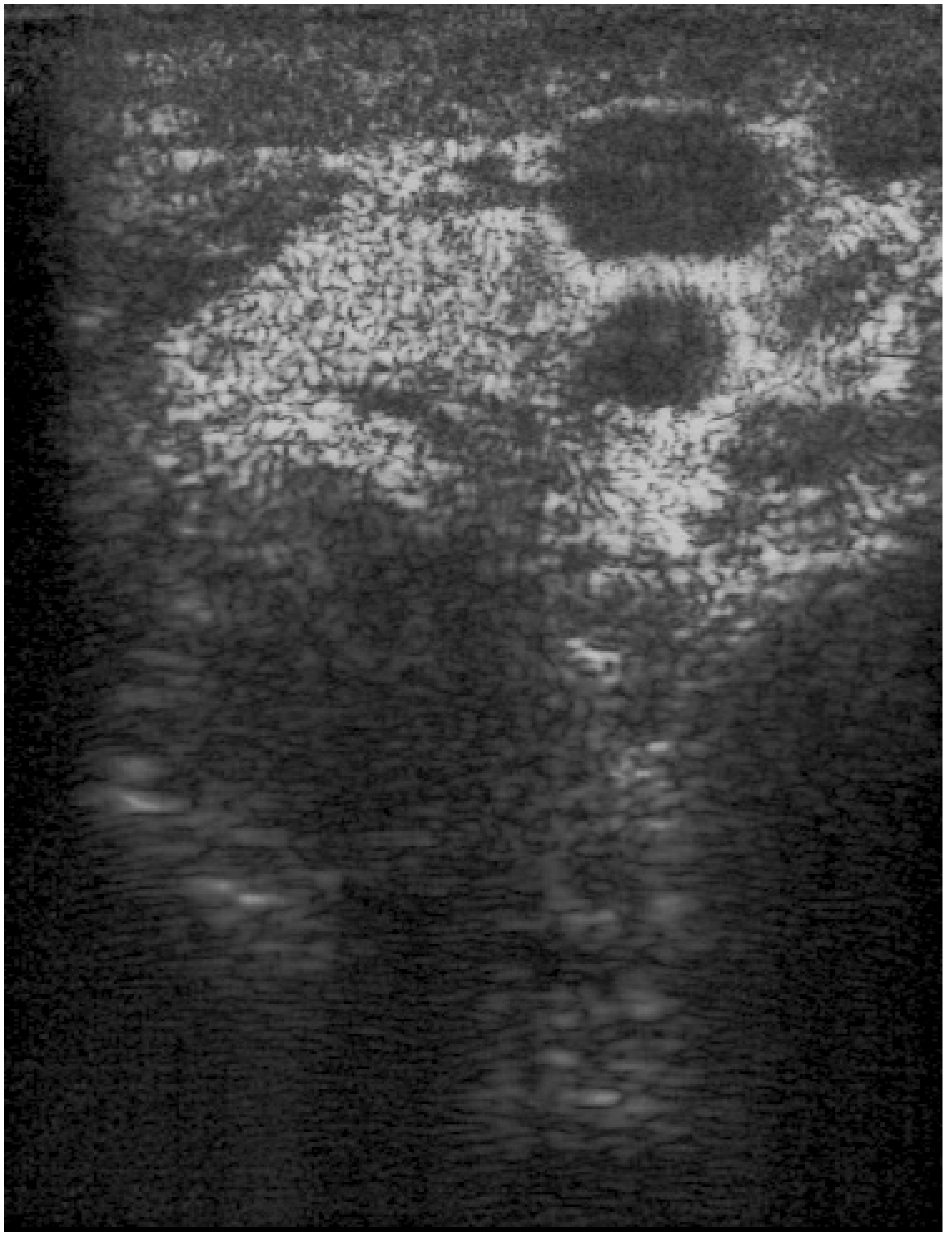

Figure 20. Ultrasound image of the right CCA and right internal jugular vein of a 25 year old female subject.

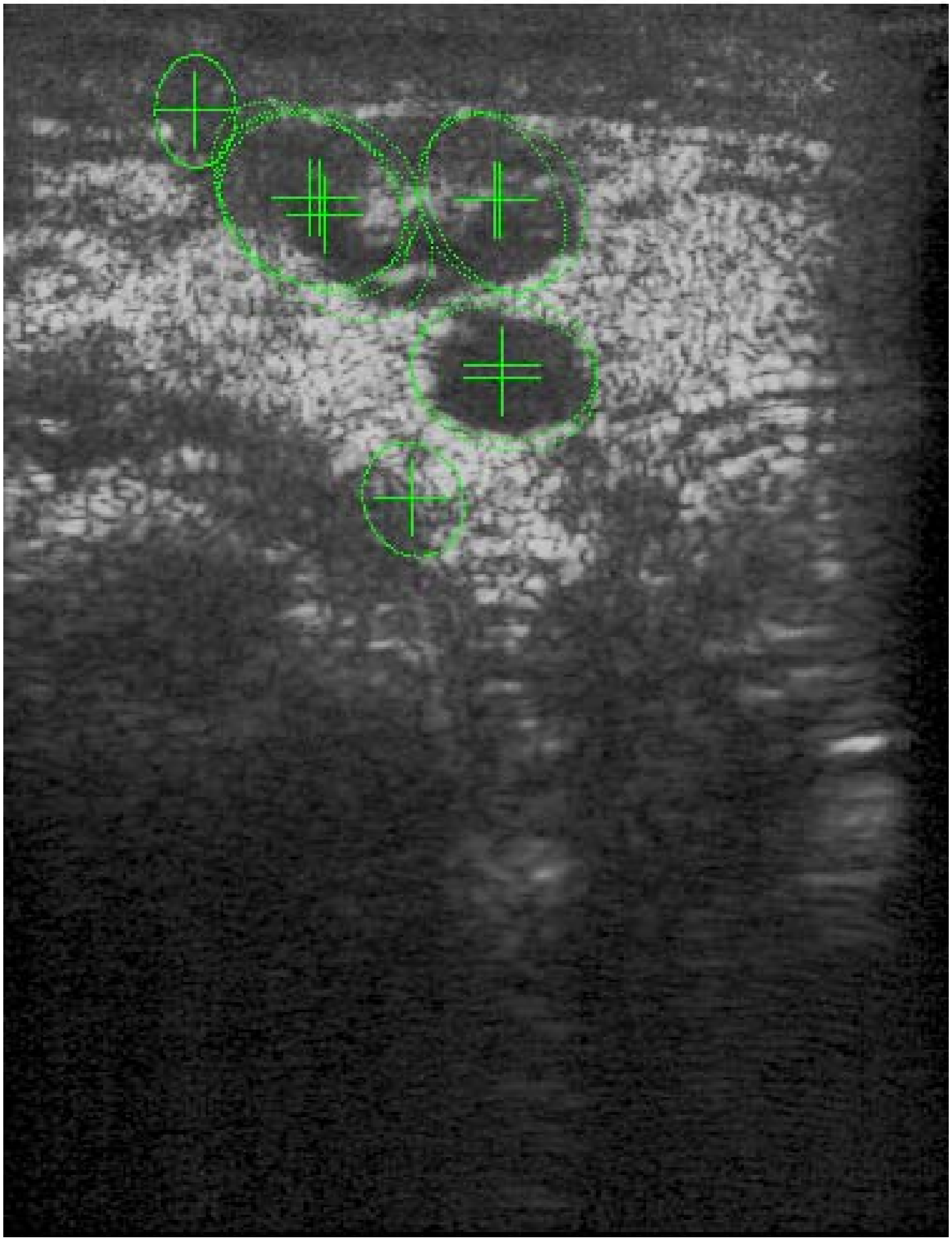

Figure 21. Brute force search for ellipses in the subject described in Figure 20. The ellipses with centers marked by plus signs are shown here in green (or white if this page is printed in grayscale).

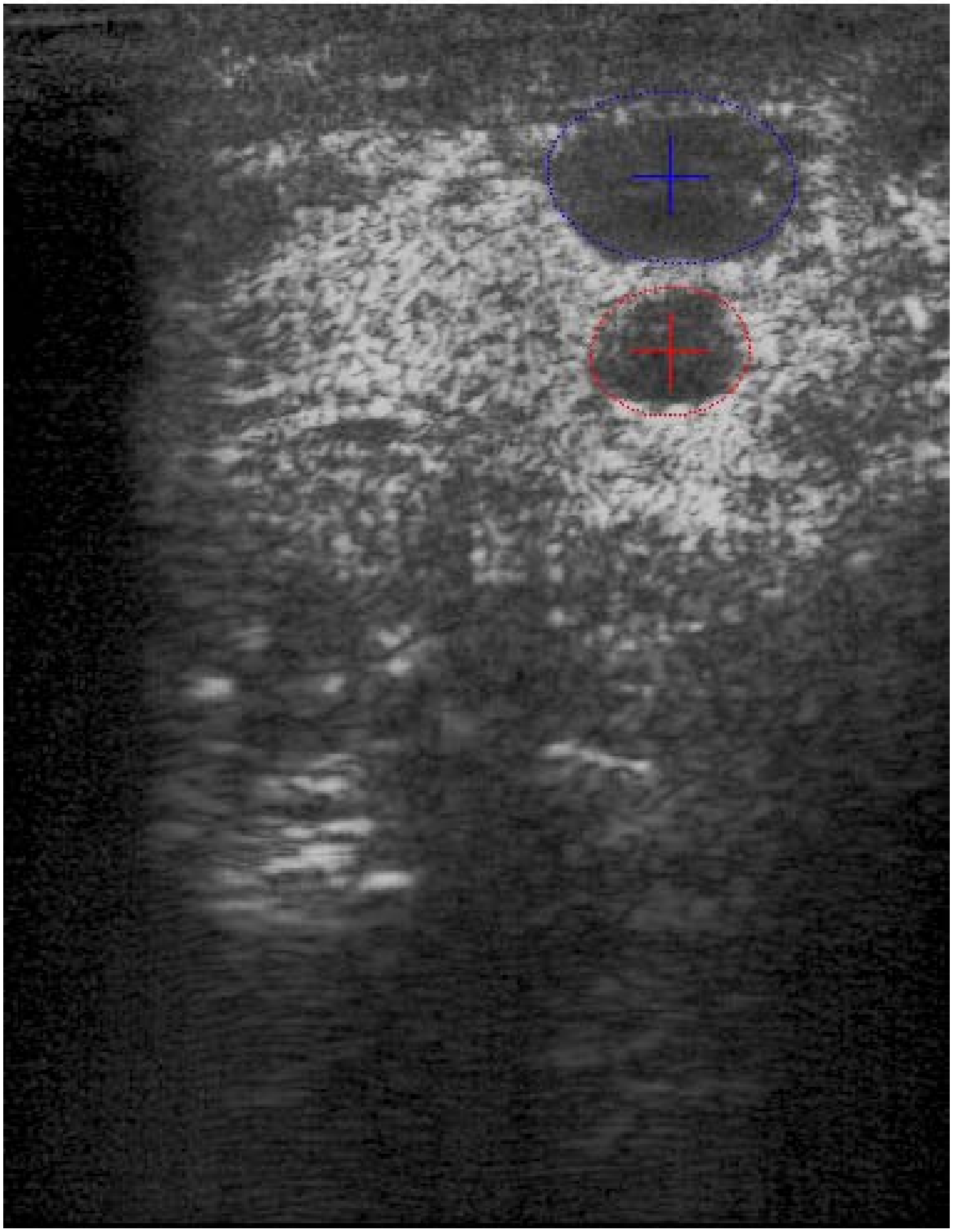

Figure 22. Final classification of the internal jugular vein (top, in blue) and CCA (bottom, in red) in the subject described in Figure 20. (If this page is printed in grayscale, both ellipses would show up in black)

9.2. Confidence Level

As the sum of the weighted parameters approaches 0, we are less certain of its corresponding vessel classification. By the same reasoning, as the sum approaches positive or negative infinity, we should be more certain of its classification. However, we remain cautiously doubtful when the sum deviates too much from the bi-modal distribution. We have chosen one standard deviation from each permutation cluster centroid to be our threshold. If the sum is too close to 0, we mark both vessels green. If the sum is within that one standard deviation, we mark the vessels blue and red appropriately. If the sum is too far from 0, we mark them light blue and pink. The significance of this latter form of non-confidence remains to be examined.

Chapter 10. Future Work

10.1. Limitations

We have yet to exhaust our search for features that can reliably distinguish between the CCA and the IJV in B-mode ultrasound. For example, we have found that combining the above Fisher's linear discriminant analysis with expected relative vessel depth can produce a more robust system, and perhaps a system could be devised for using vessel depth when it appears the scan has been performed in an appropriate section of the neck where the vessels are not side-by-side. In addition, we believe the methods that we used to identify the vessels could also detect patterns of pathology based on ultrasound scans of the CCA and IJV. So far we have only focused on features that can be derived with minimal computation to allow the system to run in real-time. The carotid and jugular waveforms actually exhibit minor peaks and troughs within its broader sinusoidal waveform as shown in Figure 7. These complex yet subtle features are termed the x and y descents. With advances in computing technologies, the x and y descents within the carotid and jugular waveforms can be identified and used for classification purposes. In addition, speckle tracking, which is currently cumbersome to compute, may become practical with greater computation speeds for tracking vessels that pulsate or as the probe moves about the neck.

Our training set of subjects is not representative of the patients needing jugular catheterization. The subjects were young and healthy, with no known stress factors.

Patients with cardiovascular problems will likely not have vascular features that fall within the values of our training set. Therefore, a larger and more representative population of subjects should be used to train the actual clinical system, and we can expect in increased variance in this population.

The *Spokes Ellipse* algorithm requires steady manual ultrasound scanning over a period of time. This may or may not be possible in a clinical setting, especially if the patient is not already sedated. Other practical issues may arise during actual clinical trials of the device.

10.2. Clinical Trials

The best way to evaluate how these limitations can affect the utility of our CCA and IJV tracker and identifier is by using the system on patients. We are currently submitting an application to the University of Pittsburgh Institutional Review Board to obtain approval for using this system on patients who are undergoing IJV catheterization. We plan to run our system in the background and validate the vessel markings, before ever presenting it in real time to the clinician for actual use in guidance. We also plan to store the ultrasound video stream and use it to augment our training set.

10.3. Vascular Pulsation Phase Differences

In our quest to identify consistent differences between the CCA and IJV, we have discovered that the pulsation phase differences between them are quite consistent. To our knowledge, our system is the first to quantify such phase differences by analyzing ultrasound images of the CCA and IJV. We expect our calculated phase differences to be the norm in healthy individuals in their 20s in the relaxed atmosphere of our experimental conditions. Since phase differences are a direct consequence of the cardiac cycle, we can expect deviations from our calculated norms to be potential causes of concern as they may signal underlying cardiovascular pathologies.

10.4. Spokes Ellipse Algorithm Applied to Other Vessels

Having shown that the *Spokes Ellipse* algorithm can reliably track the CCA and IJV, we believe we can extend its application to other vessels, namely the subclavian and femoral arteries and veins where accidental puncture of the wrong vessel is also common, and where the results, though less often fatal, can still be very serious. We can also use the algorithm to compute features that may signal pathologies on these vessels as well, but, again, data collection on real patients will be necessary to determine the normal and the pathological ranges of values.

Appendices

A. Sonic Flashlight Related Projects

Many projects other than image analysis branch from the SF concept. The ones I worked on include building a laser needle guide [40] for the SF, ways to account for refraction during calibration, engineering designs to improve image quality [48], and applications in scaled telesurgery [50-51]. These are included here as appendices, since they were not part of my proposal, but do represent related work that I accomplished during the years of my doctoral training in the Visualization and Image Analysis Laboratory.

I. Laser Needle Guide

a. Background

In ultrasound-guided vascular access, it is often necessary to insert a needle outside the plane of an ultrasound scan. Because, in such cases, the tip of the needle is not visible until it reaches the ultrasound scan, a potential exists for the needle to miss the target, requiring multiple needle insertions and unnecessary trauma to the patient. Even with the Sonic Flashlight, such through-plane insertions rely on perceptual extrapolation of the needle path, which is prone to some error [67-70]. Hence a method to accurately guide the needle to the target by “homing in on it” even when not in plane would be valuable.

Typically, needle guides are attached to the ultrasound probe and restrict the needle to travel along a specific path within the ultrasound plane. They have been routinely used to perform needle biopsies of various organs, including the liver, kidney, prostate, and breast [41-44]. The needle pathway is indicated on the monitor by means of guide lines superimposed on the ultrasound image. While steerable in-plane needle guides are currently being developed [45], the needle is still restricted to travel in the scanning plane.

Needle guides have also been developed to operate out of the plane of the ultrasound scan. Two commercial systems are currently available. The PunctSURE™ vascular access imaging system (Inceptio Medical Technologies, L.C., Kaysville, Utah) is a variation on traditional ultrasound systems, presenting real-time cross-sectional and longitudinal B-mode scans simultaneously on the display side by side. With the vein centered in the cross-sectional scan, the longitudinal ultrasound array is properly oriented parallel to the vein. The needle, when inserted in the plane of the longitudinal scan, can be visualized in its entirety, and no needle guide device is needed with the system.

The second system is the Site-Rite™, (CR Bard, Murray Hill, New Jersey) in which an out-of-plane needle guide attaches to the ultrasound probe, restricting the needle to a pathway that intersects the ultrasound scanning plane at specific depths, ranging from 0.5 cm to 3.5 cm, in 1 cm steps. The choice of depth depends on which of 4 disposable needle guides is attached to the probe. After guiding the needle into the vein, the guide can be separated from the needle, facilitating insertion of a catheter.

Both guidance systems suffer from a lack of perceptual coupling between the act of needle insertion and visual feedback from the ultrasound image, with the display located separately from the transducer. With the PunctSURE system, the user can follow the needle trajectory, but must look away from the site of operation in order to do so. Such displaced hand-eye coordination causes attentional shifts and may introduce errors and variability in the operator's performance. The mental imagery involved in locating the target is a demanding cognitive process, subject to error. The Site-Rite permits prediction of the needle trajectory, but restricts the insertion to a fixed number of pre-determined angles, depriving the operator of the ability to perform insertions along an arbitrary path.

Another experimental needle-guidance system uses a 3D ultrasound machine with computer analysis to locate the needle [46]. Others required placing radio-opaque markers on the skin, CT-scanning, 3D segmentation, stereo-cameras, and tracking devices to localize the needle [47]. These systems are cumbersome and require extensive individualized calibration.

b. Method

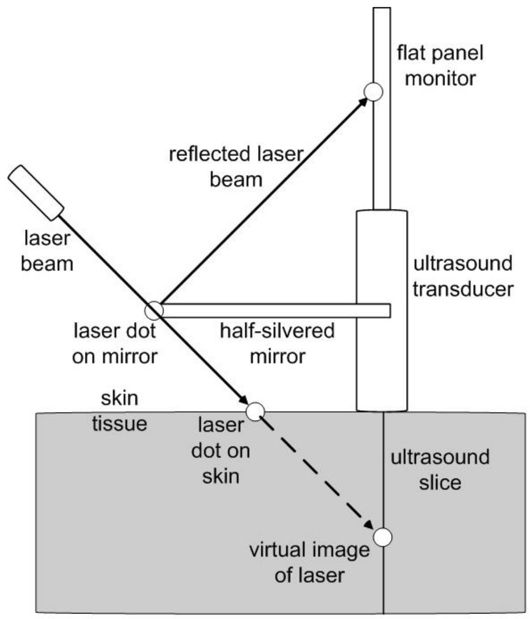

Figure 23. Laser Needle Guide optics overview

We have applied the concept of *Real Time Tomographic Reflection* (RTTR) to produce a new method of needle guidance, capitalizing on the fact that the optical geometry of RTTR works as well for light hitting the display as coming from it. If a low-intensity laser is aimed at a target in the virtual image, it can be used to define a straight path for needle insertion. As shown in Figure 23, if the laser beam hits the mirror, it will both reflect and pass through. The part that passes through the mirror will create a light spot on the skin, which shows the point the needle would enter the body along that trajectory. The part of the laser beam that reflects off the mirror will create another light spot on the flat panel monitor at exactly that point in the image displaying the target. As the image on the flat panel monitor reflects off the half-silvered mirror to create a virtual image, a reflection of the laser spot also shows up in that virtual image at the actual location within the patient where the needle will intersect the ultrasound scan.

In order to have the laser beams strike as closely as possible to the needle destination, we place the laser generators parallel to, and as close as possible to, the needle. As shown in Figure 24 two lasers are used so that the mid-point of the two spots in the virtual image flank the destination of the needle. Since the lasers must reflect off the half-silvered mirror, the needle is positioned in a small notch cut into the edge of mirror.

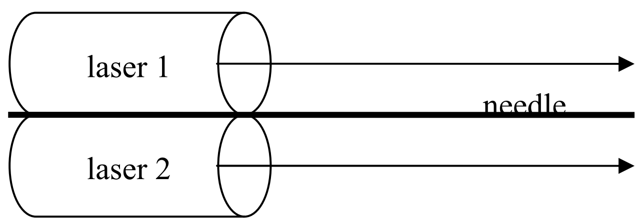

Figure 24. Positional relationships between the two lasers and the needle

c. Results

We have tested two implementations of the laser needle guide. In the first implementation, we used an older SF prototype (Model 4) to guide the insertion of a needle into a water tank to hit a small spherical target mounted in the tank. The water surface in the tank was covered with loose screening, which permitted penetration by the ultrasound beam and the needle. As shown in Figure 25, each of the lasers generates four pairs of bright spots, labeled 1-4 (the spots are red if you are reading a color version of this paper). The needle is difficult to see in the darkness, but was inserted into the tank to hit the target, while maintaining contact with a notch in the edge of the mirror. Following the paths of the laser beams, the four pairs of spots are as follows: The laser beams traverse the lower half of Figure 25 from left to right, striking the mirror (4) and splitting into two beams. The upper (reflected) beams reach the flat panel monitor (1) while the lower beams penetrate the mirror to product bright spots on the surface of the water covered by white screening (3). The virtual image (2) of the spots on the flat panel monitor (1) accurately flank the target at its actual location in the water tank. The photograph does not convey the strong perceptual depth of these spots felt by the observer. By keeping the lasers aimed on either side of the target, we successfully and easily reached the target with the needle.

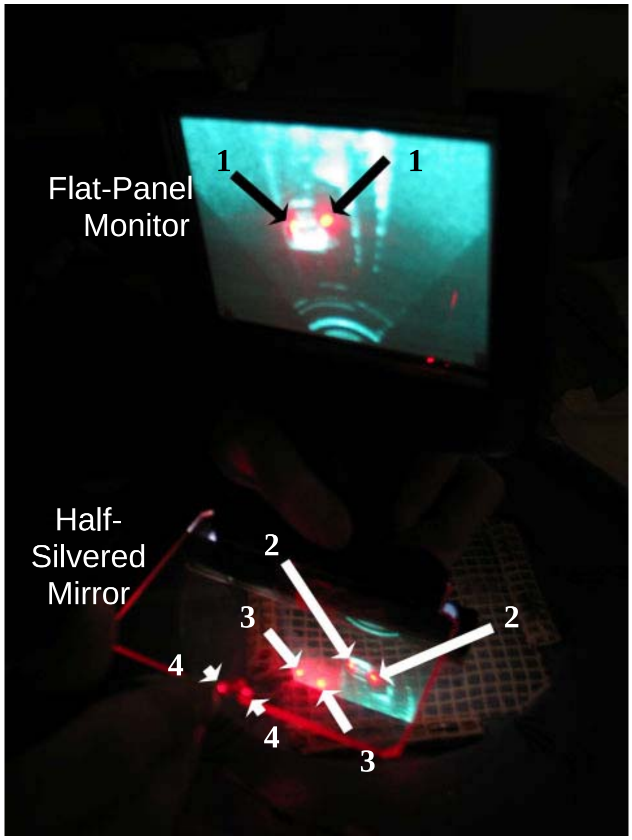

Figure 25. Using a two-laser needle guide with the Model 4 Sonic Flashlight (see text)

In the second implementation of the laser needle guide, we used a more recent prototype of the SF (Model 6), which is more compact and produces higher quality ultrasound images than the Model 4. In this case, a gel phantom containing a simulated vein was used as a target. Although a clear photograph of this apparatus in operation proved difficult to obtain, it was nonetheless easy to use. When we penetrated the phantom and pushed the needle toward the target, the needle bent slightly, changing its course. Since the lasers do not bend, the needle became misaligned with the laser. This problem could be solved by using a stiffer needle or an unbendable biopsy gun.

d. Discussion

We have demonstrated the feasibility of the two-laser needle guide with the SF. Whereas the SF with unaltered needles has shown good accuracy for relatively shallow targets such as veins in the arm, the addition of laser guidance may be appropriate for deeper procedures such as biopsies of the liver or kidney. The longer needles required for deeper procedures would lend themselves nicely to the apparatus, given the requirement that they maintain contact with the edge of the mirror.

Several areas for potential improvement could be addressed. First, we would like to eliminate the laser spot visible on the half-silvered mirror itself, due to scattering within it and on the mirror's surface. This spot is of no particular use and may be a potential distraction. The solution is to keep the mirror surface clean so as not to scatter light, and perhaps to find a different type of mirror that minimizes internal scattering. Another area for improvement is the specular surface of the flat panel monitor. Ideally we want the monitor to scatter the laser beam to create a red spot instead of reflecting (or absorbing) it. This could be accomplished by adding an antiglare diffusive surface. Finally, we are considering various schemes for reducing the number of lasers from two to one so that the needle ends up being in the center of the laser beam.

Since lasers are involved in this system, a safety analysis of potential damage to the retina is warranted. A number of paths for the laser light are created by reflections. Although the light attenuates at each of these, potential danger still exists. Our present apparatus uses two Class 3B lasers, which should not be viewed directly or in a specular reflection, but normally will not produce a hazardous diffuse reflection. Therefore the safe operation of the apparatus will depend on eliminating direct paths or specular reflections to the eye of the operator or patient.

II. Refraction Considerations in Calibrating the Sonic Flashlight

a. Background

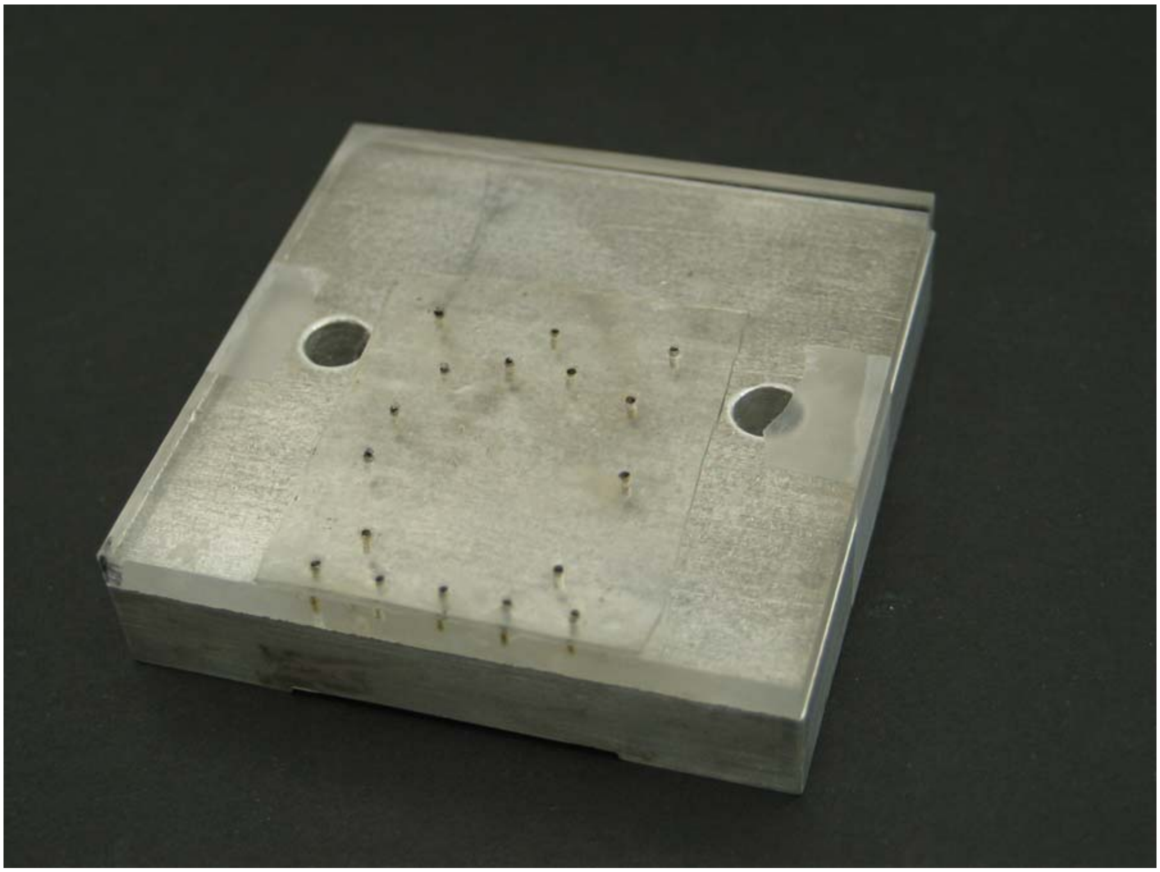

Figure 26. The thin gel phantom with small embedded targets

The most important feature of the SF is that, ideally, the virtual image appears exactly where the ultrasound image is being acquired. A reliable method of calibration is thus required. The thin-gel calibration system (Figure 26) was originally developed by Wilson Chang in our laboratory for this purpose [72]. It uses a thin layer of transparent gel phantom material with small embedded targets along which the US machine scans

(Figure 27). During calibration, the operator can simultaneously see these targets as well as the superimposed virtual ultrasound images of the targets. To perform calibration, the operator visually lines up the US image of the targets with the direct view of the targets by adjusting the location, anisotropic scale, and orientation of the US image. The process involves sequentially lining up 3 targets in the thin gel phantom from which an affine transform is computed for transforming the ultrasound image onto the flat-panel display. This affine transform represents the end product of the calibration process [72,73].

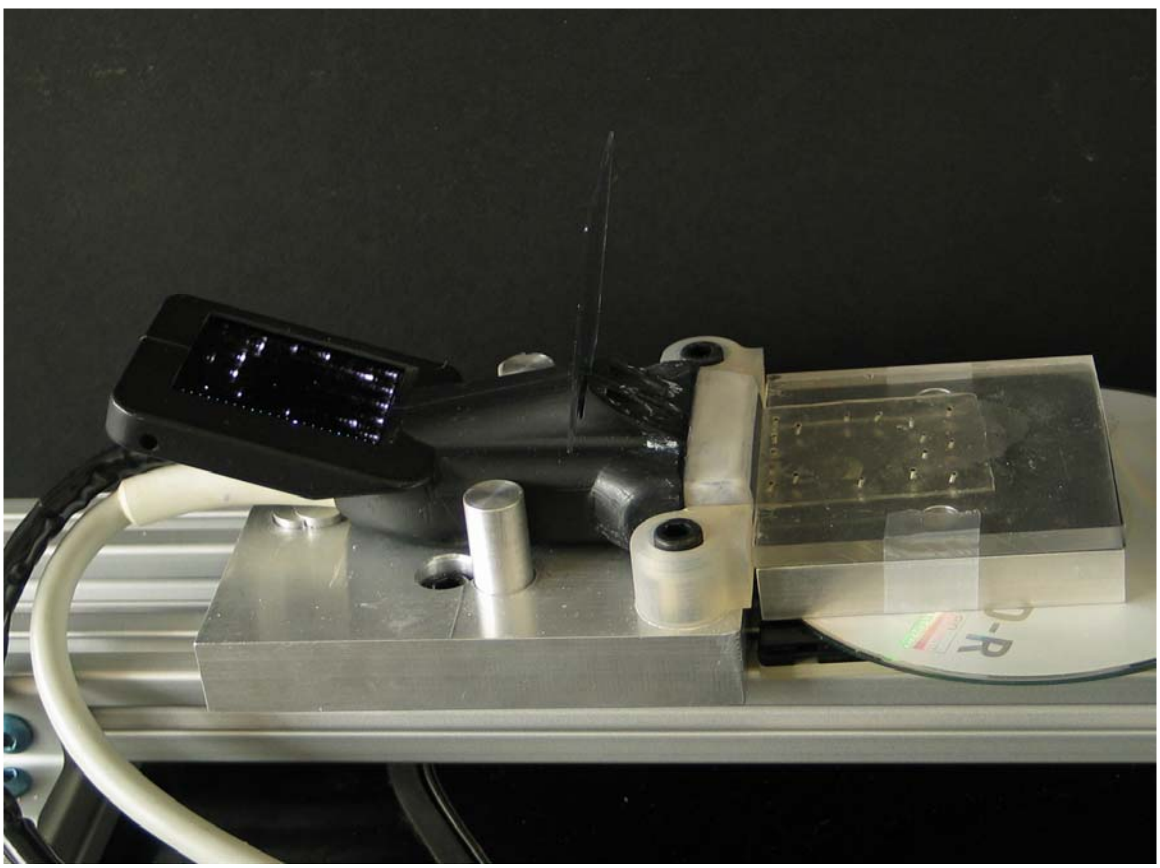

Figure 27. The Sonic Flashlight showing an US scan of the phantom.

There are a number of ways in which registering the virtual image of the ultrasound scan may not be perfect. The speed of ultrasound in tissue varies with its density and compressibility, with a maximum variation of roughly 5% in soft tissue. This causes errors in distance as well as in the direction of the ultrasound beam due to refraction. In general, such errors are assumed to be less than 1 mm over the 2 cm range of SF's field of view.

Another error can be caused by refraction by the mirror. This error was quite small with our Model 6 SF, which used a permanently installed 1 mm thick glass mirror. However, upon converting to the disposable mirror assembly, we needed to use plastic mirrors. To achieve acceptable flatness in the mirror (a potentially even greater source of error) we needed to move to 2 mm thick mirrors. These produced an appreciable amount of refractory error, which needed to be addressed before moving forward with the clinical trials that were my responsibility in the SF project. Thus I became engaged in understanding, measuring, and compensating for this error as described below.

The distortion due to refraction is dependent on the angle of observation – the larger the angle of incidence to the mirror, the larger the refraction. This error can mislead the operator during use of the SF causing misplacement of a needle. What is more, refraction can also cause errors during the calibration that can propagate into large errors during subsequent use of the SF.

To correct for this, during calibration the operator needs to modify his perceived location of the targets in the thin-gel phantom to offset for the consequences of refraction. Fortunately, since the calibration apparatus is fixed in terms of relative angles between its various components, as long as we also know the observation angle, the amount of refraction can be calculated.

An important insight in this is that we are aiming to make the virtual image appear in the correct location, but have no control over diffraction error in the direct view of objects through the mirror. This, luckily, has no effect on the perceived location of clinical targets such as veins or tumors. Unlike thin-gel phantoms, the patients' skin obstructs the direct view of such targets during clinical use of the SF. While the operator will see the patient's skin through the half-silvered mirror, it is not critical for the skin to be perfectly aligned. The operator will also need to see the needle, of course, to visually extrapolate its course, but much of that perception may be achieved by seeing that portion of the needle seen directly and not through the mirror at all.

In the next section, we will explain the methods employed to calculate the refraction error given fixed observation angles as well as the maximum refraction error when the angles are not fixed.

b. Calculating Vertical Refraction

In our treatment of refraction error, we found it useful to isolate the vertical refraction error first, and only then to incorporate horizontal error. As shown in Figure 28, the vertical error can be analyzed as a series of distances d, heights h, and angles θ. *The mirror and thin-gel phantom are seen from the side in roughly the same configuration as Figure 26.* we can easily measure d_1 and h_{123} (sum of h_1 and h_{23}). Using the laws of trigonometry, we can calculate the angle of incidence θ_i from the triangle formed by d_1, h_{123}, and the angle between them.

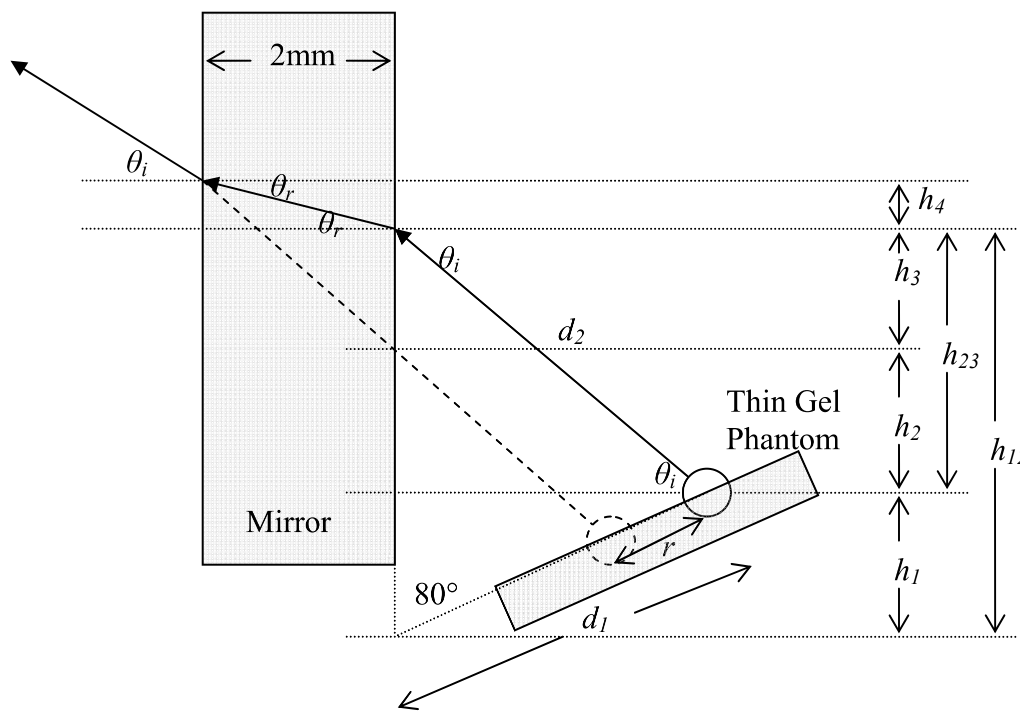

Figure 28. Diagram of refraction of light through the half-silvered mirror.
The solid circle represents the location of the actual target while the dashed circle represents the location of the perceived target. Note that the thin-gel phantom and the mirror form an 80° angle due to the geometry of the Model 7 Sonic Flashlight..

Using the cosine rule, we can calculate d_2.

$$d_2^2 = h_{123}^2 + d_1^2 - 2 \times h_{123} \times d_1 \times \cos(80°) \tag{11}$$

Using the sine rule, we can calculate θ_i.

$$\begin{aligned} \sin(90° - \theta_i) &= {d_1 \sin(80°)} \big/ {d_2} \\ \theta_i &= 90° - \sin^{-1}\left[\frac{d_1 \sin(80°)}{\sqrt{h_{123}^2 + d_1^2 - 2 \times h_{123} \times d_1 \times \cos(80°)}}\right] \end{aligned} \tag{12}$$

Using Snell's Law and assuming the index of refraction is 1.49 for the mirror (acrylic) and 1.00 for air, we can also calculate the angle of refraction θ_r.

$$\begin{aligned} 1.00 \sin(\theta_i) &= 1.49 \sin(\theta_r) \\ \because \theta_r &= \sin^{-1}\left(\frac{\sin(\theta_i)}{1.49}\right) \end{aligned} \tag{13}$$

Using the laws of trigonometry again, we can calculate h_3 as follows:

$$\begin{aligned} h_4 &= 2 \tan(\theta_r) \\ h_3 + h_4 &= 2 \tan(\theta_i) \\ \because h_3 &= 2[\tan(\theta_i) - \tan(\theta_r)] \end{aligned} \tag{14}$$

Finally, using the laws of similar triangles, we can calculate the refraction r.

$$\frac{h_3}{h_{123}} = \frac{r}{d_1}$$
$$\because r = \frac{d_1 h_3}{h_{123}} \tag{15}$$

Three particular targets in the thin-gel phantom are routinely used for calibration because they form one of the largest triangles in the phantom, yielding the greatest accuracy when establishing the affine transform for calibration. The refractions, after fixing the angle of observation to approximately 26.6°, are 0.211 mm, 0.179 mm, and 0.203 mm respectively using the equations discussed. When an operator lines up an ultrasound image visually to its actual target, our calibration software automatically corrects the ultrasound image of the targets by the specified amounts to account for refraction before calculating the affine transform.

c. Expected Refraction in Clinical Use

During clinical use of the SF, refraction will occur to anything viewed through the mirror, such as the skin of the patient or the portion of the needle viewed through the needle. A schematic of this is shown in Figure 29.

To view the entire virtual image, the operator can only look through the mirror at a maximum of approximately 30° vertical and 30° horizontal angles. The vertical and horizontal angles effectively increase the mirror width for each other for the purpose of calculating refraction. Using 30° as angle of incidence, we can calculate the angle of refraction

$$1.00\sin(\theta_i = 30°) = 1.49\sin(\theta_r)$$
$$\because \theta_r = \sin^{-1}\left(\frac{\sin(30°)}{1.49}\right) = 19.6° \tag{16}$$

We can then calculate the length of the path that the light must travel within the mirror.

$$\cos(\theta_r) = \frac{2mm}{length\_of\_light\_in\_mirror}$$
$$length\_of\_light\_in\_mirror = \frac{2mm}{\cos(\theta_r)} = 2.12mm \tag{17}$$

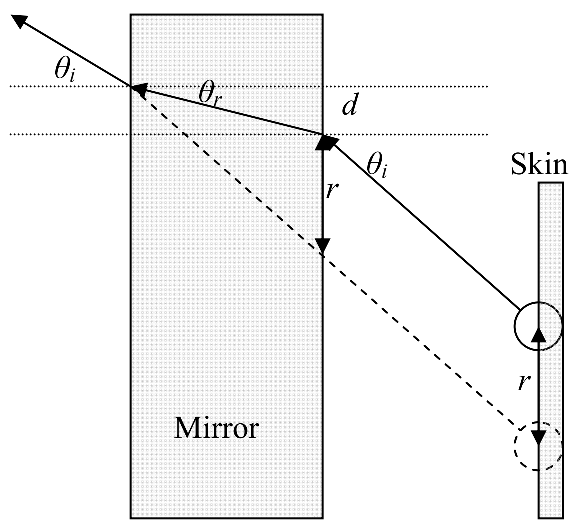

Figure 29. Schematic of the refraction of light through the mirror when viewing the skin through the mirror.

Consider 2.12 mm as the new mirror width for either the vertical or horizontal viewing angle; we can calculate the refraction *r* along either the vertical or horizontal direction.

$$
\begin{aligned}
&\tan(\theta_r) = \frac{d}{2.12mm} \\
&\tan(\theta_i) = \frac{d+r}{2.12mm} \\
&\because r = 2.12mm \times \tan(\theta_i) - 2.12mm \times \tan(\theta_r) = 0.47mm
\end{aligned}
\tag{18}
$$

The maximum refraction for any point on the skin is thus 0.47 mm in the horizontal direction when the horizontal viewing angle is 30° and the vertical viewing angle is 0°. Similarly, it is also 0.47 mm in the vertical direction when the vertical viewing angle is 30° and the horizontal viewing angle is 0°. We consider this tolerable for errors in the location of targets viewed directly through the mirror.

III. Solution to SF Image Distortion due to Probe Cover

The initial SF clinical trials were conducted with the Model 6, whose permanent mirror was required to be inside a plastic probe cover. The inconsistent optical properties of the probe cover (Figure 30), which enveloped the entire SF device to ensure sterility, distorted the image. Figure 31 shows the same SF view but without the probe cover. Image blurring was specifically considered an impediment by our radiologist during 3 out of the 15 procedures performed with the Model 6.

Although the plastic probe cover (Bard Access Systems, Salt Lake City, UT. Part#9001C0197) was rated by the company as "transparent," it still acted as a diffuser and caused image blurring. Light emitted from individual pixels of the flat panel display traveled some distance before being diffused by the plastic probe cover. It was this diffused light that reached the eyes of the operator, blurring the image. If, instead, the plastic could be held tightly against the display, diffusion would be expected to cause far less blurring of the image. Following this logic, we created a separate disposable sterilized mirror holder that snapped onto the flat panel display (Figure 3), holding the plastic probe cover flat inbetween (Figure 4). An optional hood could be snapped onto the entire apparatus to reduce reflection from ambient light.

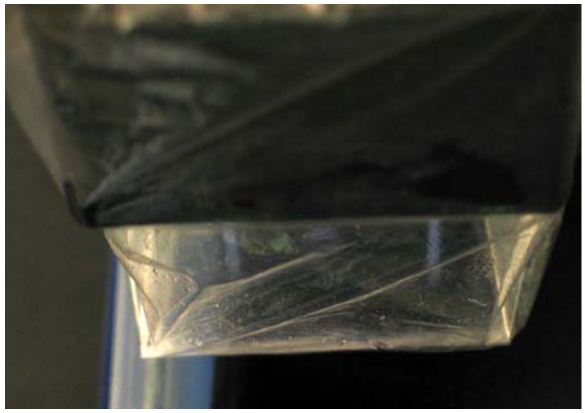

Figure 30. Virtual image seen through the half-silvered mirror with the plastic probe cover. Note the increased blurriness compared to Figure 31 (though this is, in part, due to the camera being focused on the plastic bag).

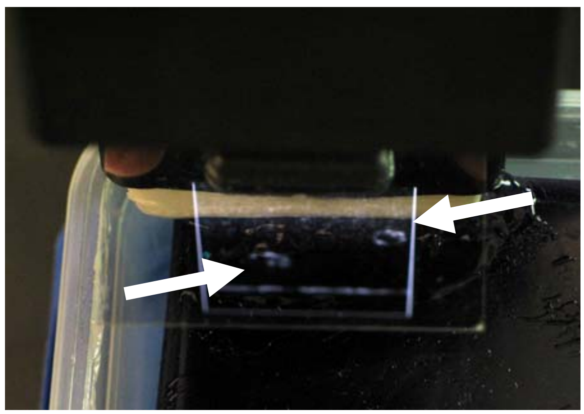

Figure 31. Virtual image of two simulated vessels (arrows) in a phantom seen through the half-silvered mirror without the plastic probe cover. The same vessels were present in Figure 30 but not clearly visible through the plastic probe cover.

The resulting image (Figure 32) appeared as if the plastic probe cover had no light distorting effect, allowing for a great improvement in this crucial element of the SF. This version of the SF, the Model 7, is currently what we use in our clinical trials.

The main disadvantage of this modification, however, is that the mirror and the hood are now unprotected by the probe cover. They have to be sterilized for each patient.

To further eliminate the risk of cross-patient contamination, the mirror holder and the hood are disposed of after each procedure. We have worked with a commercial company to mass produce these plastic mirror holders and hoods using an injection molding process.

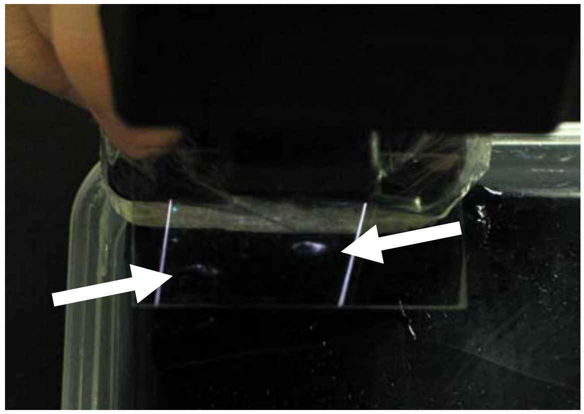

Figure 32. Virtual image of two simulated vessels (arrows) in a phantom seen through the half-silvered mirror with the plastic probe cover held tightly on the surface of the flat panel display by a sterilized disposable plastic mirror assembly.

An added concern with the disposable mirror assembly is consistency of precision. In particular, mirror angle is a concern, since an imprecise angle results in a dislocated virtual image. It was discovered that an improper angle during calibration has an error-multiplying effect, in that small angular errors in the calibration mirror multiply into large displacement errors along the plane of the virtual image. It behooved us to develop a special calibration mirror (Figure 33) whose angle could be carefully controlled. The error due to mirror angle during actual use of the SF still remained, however. We measured this error by having 3 different people calibrate the SF using 4 disposable mirror assemblies. The resulting calibration affine transforms were then compared to compute the maximum difference between the various locations within the virtual image where a given point could be placed. This maximum difference turned out to be 0.42mm.

In all clinical trials after the initial 15, after switching to the Model 7, the vessels were visualized with significantly greater clarity than when the probe cover obscured the images. The needle was easily aimed and inserted into the basilic or brachial vein as before. Image degradation due to the bag was no longer appreciable.

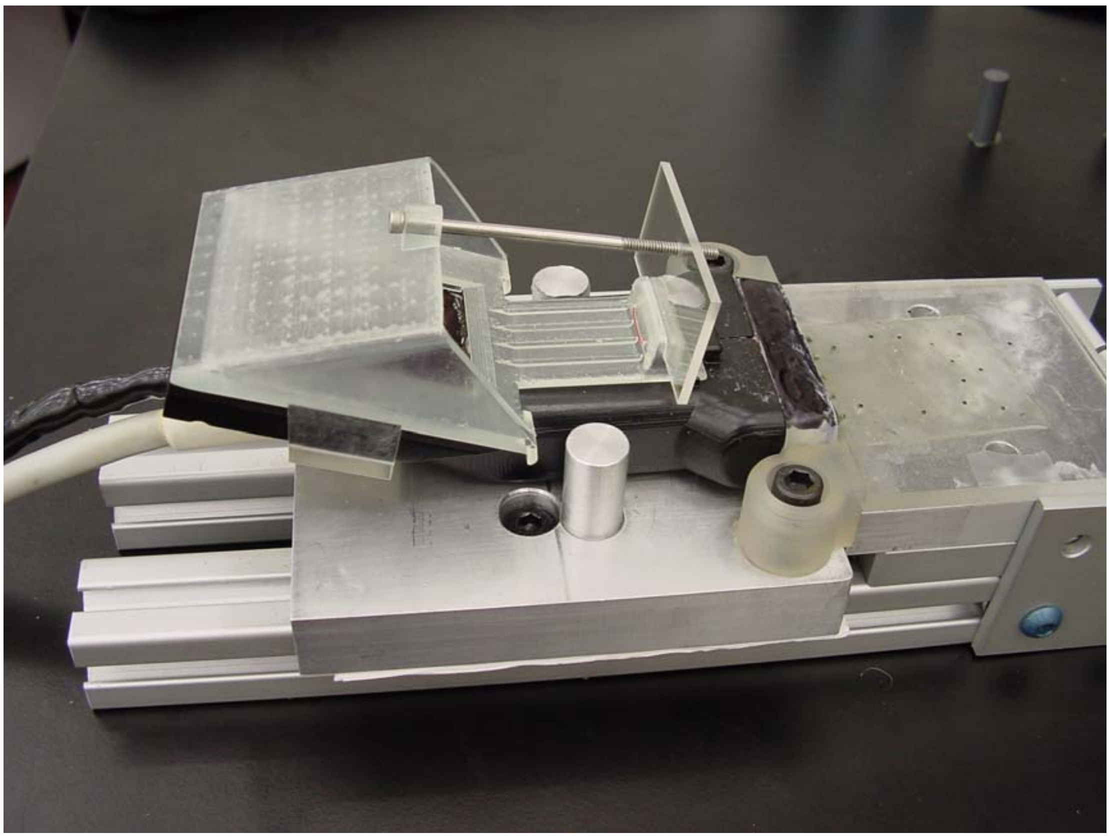

Figure 33. Special calibration mirror whose angle could be carefully controlled with a screw.

This study validated our basic design for the SF and the improvements made to it with the disposable mirror assembly. It showed that basilic and brachial venous access can be safely accessed using the SF for guidance. We believe our new disposable mirror outside the bag satisfies the requirement for sterility without significantly degrading visibility.

IV. Scaled Telesurgery

a. Introduction

I conducted this final piece of work, related to my dissertation but outside my actual proposal, in collaboration with Samuel Clanton and Yoky Matsuoka. It was published in the IEEE Transactions on Visualization and Computer Graphics [26].

Robotic assistants are currently being introduced into surgery because they hold the promise of aiding or enhancing the capabilities of surgeons to perform more effectively in certain circumstances. One class of surgical assistant is designed to transfer the motions of a surgeon to a different location and scale. These are used to establish operator telepresence for a surgeon at a remote location, to allow procedures to be conducted less invasively, or to otherwise enhance surgical performance. The purpose of our research is to create a new human interface for such systems, one that allows an operator to interact more naturally with a workspace located at a distance and of arbitrary size. Our intent is, as much as possible, to make operating at a different location and scale as easy and natural as performing more traditional local procedure..

In the present research, we extend the general approach of the SF to create a system by which an operator can employ direct hand-eye coordination to interact with a remote environment at a different scale. In the SF, an ultrasound image is registered with a direct view of the surface of the patient. In the new system, a remote effector is located in the operating field of a patient or other workspace. An image of that remote workspace, displayed at an arbitrary level of magnification, is merged with the direct view of a master instrument held by the operator and linked to the motion of the actual slave effector. The master effector is an appropriately scaled version of a manipulator handle for the slave effector, designed for optimal use in the hand of the operator. The master effector is electromechanically or otherwise linked to the slave effector such that motion of the master will cause equivalent, scaled motion of the slave effector in the remote workspace. An image of the target from the remote workspace is merged with the operator's view of the master effector in his hand, and it appears to the operator that he is interacting directly with the remote, scaled environment.

b. Method

Our prototype system, dubbed the "Telepainter," has been created as an implementation of remote *Real Time Tomographic Reflection* (RTTR)using light microscopy with an electromechanical master-slave controller. We chose to demonstrate the basic image merge and motion transfer capabilities by implementing a system with which we could paint very small pictures remotely. Although not a clinical application, painting was chosen to demonstrate remote RTTR because it is tolerant of a wide range of forces, while permitting complex hand-eye tasks to be performed.

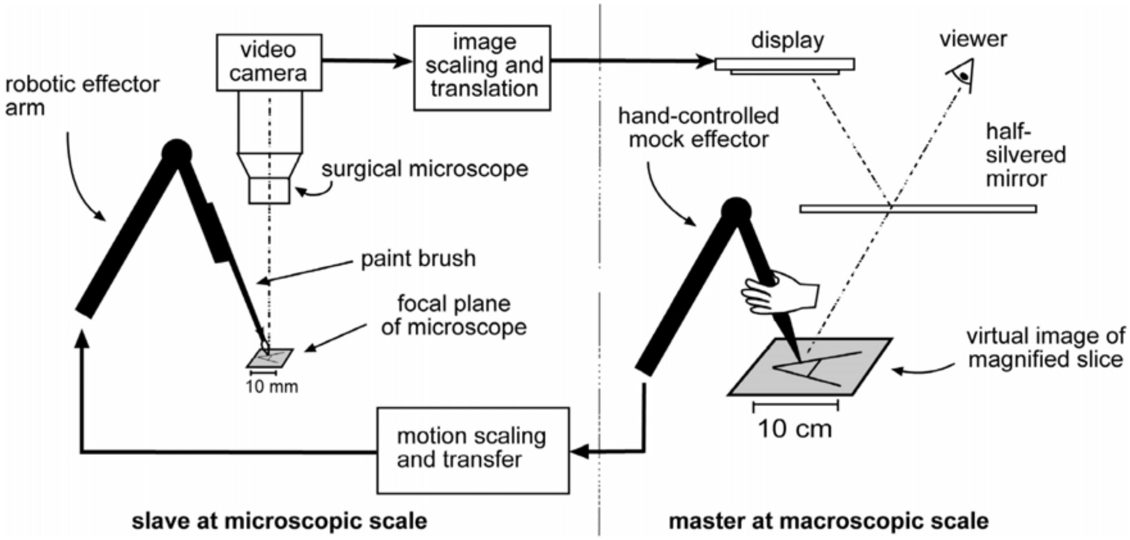

Figure 34. Apparatus for the "Telepainter" prototype. A master controller paintbrush handle ("mock effector") is linked to a slave effector paintbrush at 1/10 scale. Video images are magnified and registered with the operator's workspace.

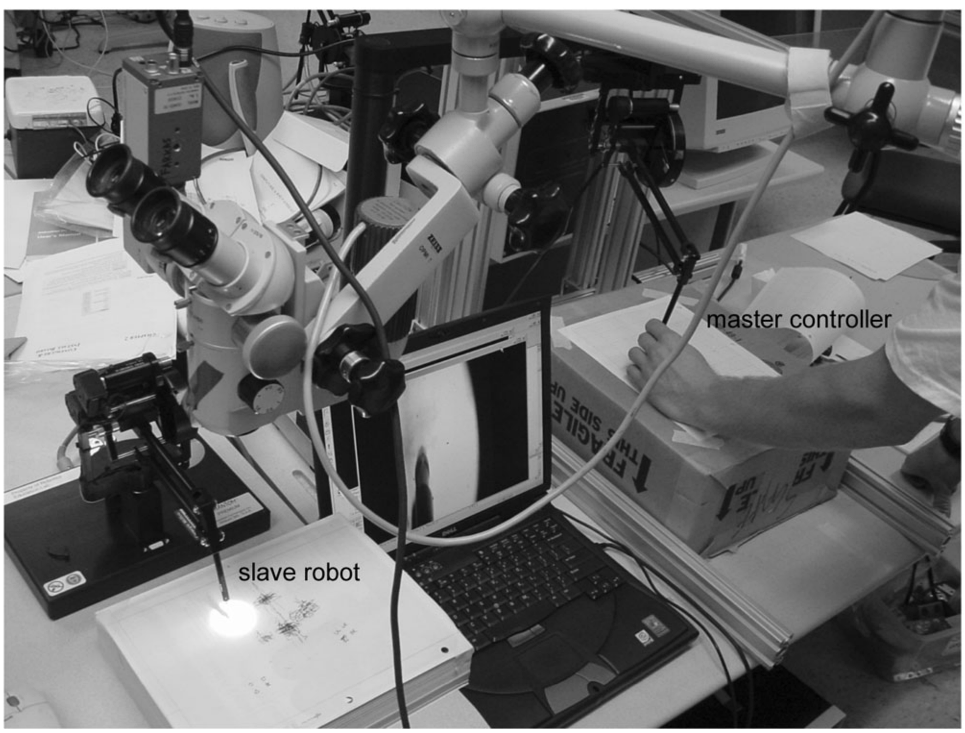

Figure 35. Telepainter apparatus showing master and slave robots. Operator is manipulating paintbrush handle held by the master (passive) robot while the slave robot is moving the paintbrush. Paper is white in this photo, though black paper was used during actual operation. The half-silvered mirror and flat-panel monitor over master controller are not shown.

In this system (Figure 34), the workspace of a small robotic arm is viewed as a video image through a surgical microscope (VDI IR Pro video camera attached to a Zeiss OPMI-1 microscope). This image is visually superimposed on the natural workspace of the operator via a half-silvered mirror (34 x 23 cm) mounted 38 cm above a piece of black paper. A master-slave system is implemented using two SensAble Technologies Phantom haptic interface devices as the master and slave devices. The slave robot arm, a Premium 1.0 model Phantom haptic interface operating with 3 active degrees of freedom, holds a small paintbrush. The master controller is a SensAble 1.5 Premium model Phantom operating passively, with 3 degrees-of-freedom joint-angle encoding, holding a paintbrush handle. The master and slave robot arms are linked such that manual movement of the paintbrush handle (master controller) by the operator produces corresponding movement by the paintbrush (slave effector), scaled down by a factor of 10. A second piece of black paper is placed within the reachable extent of the brush (Figure 36), and a small blob of tempura paint is placed on the paper (Figure 37).

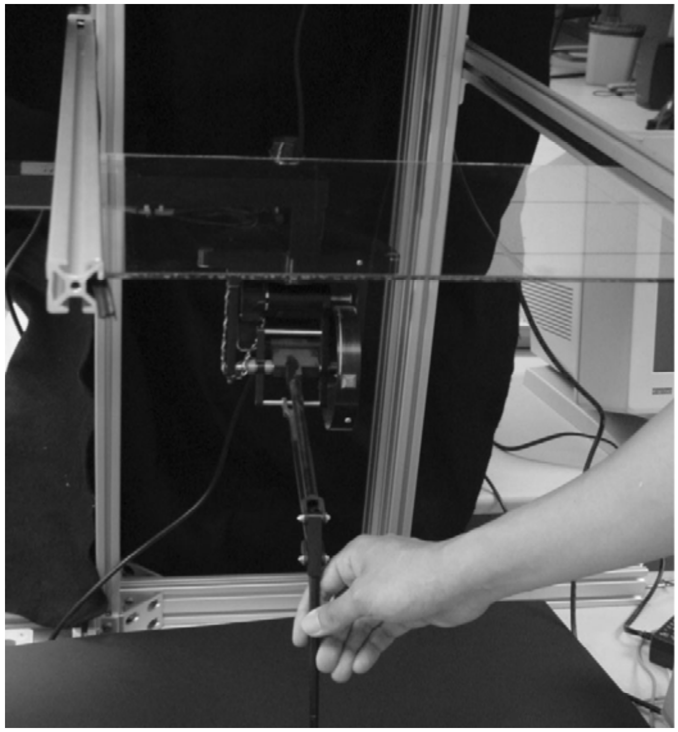

Figure 36. The master controller is seen with its paintbrush handle beneath the half silvered mirror. Also shown is the black paper in the operator's workspace (no actual paint is placed there). The flat panel monitor (not shown) is mounted above the mirror a distance equal to that between the mirror and the black paper.

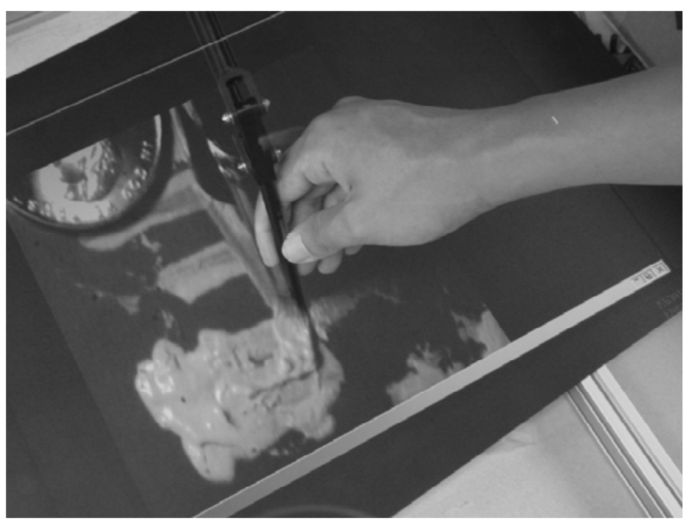

Figure 37. The Micropainter system as viewed through the half-silvered mirror by the operator, showing the master handle registered with the remote paintbrush and paint. The remote environment is ten times as small (notice the scale of the penny). I am painting my surname in Chinese.

c. Results

The system was used to perform Chinese calligraphy with a paintbrush (Figure 35), enabling the user to paint very small characters (roughly 2 cm square), among other things, while giving the impression of painting much larger characters (roughly 20 cm square). Note the relative size of the penny to the drawing in Figure 35. To the operator, it seemed that his hand and the paintbrush were connected and interacting with the paint and the paper in the remote environment.

It is interesting to note that the SensAble Technologies Phantom slave robot in the system is normally used as a haptic interface device rather than as an effector robot. To implement the scaled motion transfer feature of the system with the Phantom, a Proportional-Integral-Derivative (PID) controller was implemented to control the slave Phantom. Periodic procedures monitored the position of the input and output instruments, and a third periodic procedure used the PID controller to adjust a force on the output Phantom such that it would move to the correct scaled position. The PID parameters were adjusted so that the slave would quickly and accurately track the master. The slave Phantom consistently achieved a position within 0.5 mm of the correct scaled-down position of the input Phantom in the plane of drawing.

Since only 3 degrees of freedom were available for manipulation of the robot, only information about the tip location, without the tool orientation, could be transferred. The input and output devices were kinematically different, and working at different scales, so the orientation of the tools between robots was skewed to some degree as the tools moved to the extents of their drawing planes. Using a 7 degree-of-freedom slave robot could overcome this limitation. In addition, the image merge of the position of the tool tips in the plane of drawing was correct from any viewpoint, but the out-of-plane location of the tools was skewed at different viewpoints. This is a problem inherent to remote RTTR, due to the 2D nature of the display, which may, or may not, be counterbalanced by the advantages offered by RTTR over other methods of visualizing remotely controlled procedures.

d. Conclusions

We have demonstrated the concept of remote *Real Time Tomographic Reflection* as an effective method for superimposing visual feedback in real time on the natural workspace of the operator. By merging natural stereoscopic vision with a normal view of one's hands holding the tool, natural hand-eye coordination can be effectively exploited in a remote environment. The lack of a head-mounted display is a further attraction.

The system has possible applications in many areas of medicine, microbiology, and engineering. One can imagine a version in which forceps and needle holder motions are transferred to perform microsurgery, where an operator could manipulate individual cells with a robotically controlled micropipette, or where a machinist could perform microscopic fabrication in an engineering context. An important limitation of the current system for light microscopy is that the visual merge is only viewpoint independent in the plane of the painting. However, for 2D tomographic imaging modalities such as ultrasound or OCT, the visual merge with the master controller would remain accurate throughout the 3D workspace of the operator. Catheter based procedures and in vitro microscopic procedures are particularly appealing candidates for this technology in clinical medicine and biomedical research.

An exciting extension of this approach, currently underway in our laboratory, involves the development of a holographic version of RTTR. Replacing the half-silvered mirror with a holographic optical element would enable greater diversity in the configuration of possible virtual images.

Another possible extension involves haptics. The integration of haptic feedback into the instrument linkage would further enhance the immersive environment for performing remote interventional procedures, allowing the operator to use the integrated senses of sight, touch, and proprioception to perform the remote procedures in a natural way. This forms the basis for a new collaboration between George Stetten and Ralph Hollis in the CMU Robotics institute to develop an RTTR micromanipulator with haptic feedback.

B. Vessel Features Calculated for All 38 Subjects

Table 11. Number of eligible spokes used to fit ellipses to the vessels in each frame

Subject	Mean Spokes (carotid)	Mean Spokes (jugular)	STD Spokes (carotid)	STD Spokes (jugular)	10th percentile Spokes (carotid)	10th percentile Spokes (jugular)	90th percentile Spokes (carotid)	90th percentile Spokes (jugular)
1	21.23	25.24	1.790	1.952	19	23	23	28
2	23.91	21.73	1.644	1.558	22	20	26	24
3	21.62	23.95	1.620	1.719	20	22	23	26
4	26.16	26.11	0.824	1.370	25	24	27	28
5	24.09	26.11	2.084	1.642	21	24	27	28
6	25.18	24.84	1.786	1.862	23	22	27	27
7	24.34	25.04	1.924	1.235	22	23	27	26
8	22.36	25.00	2.222	1.428	20	23	25	27
9	24.52	25.03	1.024	1.413	23	23	26	27
10	25.67	25.99	1.799	0.953	23	25	28	27
11	25.88	24.06	1.902	1.393	23	22	28	26
12	22.64	22.95	1.857	1.522	20	21	25	25
13	23.81	23.57	1.463	1.065	22	22	25	25
14	22.93	22.76	1.711	1.587	21	21	25	24
15	23.96	24.19	1.319	1.322	22	23	26	26
16	20.37	22.23	1.828	1.414	18	20	22	24
17	21.59	25.32	1.518	2.019	20	22	23	27
18	21.61	23.68	1.587	1.142	20	22	24	25
19	19.57	22.85	1.520	1.226	18	21	21	24
20	23.99	26.53	1.625	1.690	22	24	26	29
21	22.51	22.36	1.357	0.956	21	21	24	23
22	23.79	25.37	1.701	1.678	22	23	26	27
23	19.49	24.54	1.829	1.362	17	23	22	26
24	24.27	25.33	1.381	1.334	23	24	26	27
25	20.35	24.36	2.060	1.576	18	22	23	26
26	22.52	23.03	1.824	1.565	20	21	25	25
27	20.36	21.74	1.256	1.178	19	20	22	23
28	25.69	25.27	1.194	1.235	24	24	27	27
29	21.85	22.96	1.428	1.321	20	21	24	25
30	23.16	24.87	1.762	1.051	21	24	25	26
31	25.50	24.37	1.287	2.264	24	22	27	28
32	23.95	25.90	1.904	1.294	21	24	26	27
33	25.40	24.76	1.213	1.636	24	23	27	27
34	25.41	24.42	1.404	1.248	24	23	27	26
35	25.00	25.45	1.695	1.407	23	24	27	27
36	21.48	22.01	1.092	1.002	20	21	23	23
37	24.96	24.16	1.624	1.501	23	22	27	26
38	21.87	23.90	2.072	1.445	19	22	25	26

Table 12. Area (mm^2) of ellipses fitted to the end of the spokes listed in Table 11.

Subject	Mean Area (carotid)	Mean Area (jugular)	STD Area (carotid)	STD Area (jugular)	10th percentile Area (carotid)	10th percentile Area (jugular)	90th percentile Area (carotid)	90th percentile Area (jugular)
1	2301.6	1555.0	213.7	287.8	2051.0	1218.5	2524.5	1986.4
2	1386.4	2110.7	101.4	459.7	1263.3	1503.4	1518.0	2736.9
3	1810.4	7960.9	313.1	383.9	1491.8	7508.4	2304.6	8481.7
4	1708.5	751.3	166.0	232.6	1502.6	453.7	1902.1	1053.3
5	1525.2	3058.9	466.7	365.4	900.5	2652.5	2051.3	3483.7
6	1805.3	6413.4	321.8	647.7	1417.7	5564.8	2250.2	7252.6
7	2117.5	4801.8	537.8	772.7	1494.1	3932.2	2888.0	5669.7
8	1575.8	6506.5	391.4	495.3	1181.3	5894.4	2118.6	7170.7
9	1561.3	2578.4	183.1	332.0	1318.6	2118.7	1785.2	2987.0
10	1821.3	3856.9	255.1	173.2	1533.0	3648.1	2113.5	4079.4
11	2139.7	5850.7	220.4	649.5	1911.2	5104.5	2415.5	6638.6
12	2403.1	4584.0	311.6	1215.8	1963.8	2666.6	2793.0	5805.3
13	1447.0	4688.6	469.5	521.1	854.8	4019.4	2084.3	5395.7
14	2684.0	8183.2	278.8	583.8	2346.6	7463.1	3042.2	8795.3
15	987.3	1396.2	101.4	262.3	875.2	1071.5	1116.7	1775.0
16	1976.8	3040.6	324.7	287.3	1661.7	2643.5	2355.1	3402.7
17	2058.1	8956.0	292.3	518.3	1694.8	8303.6	2439.7	9632.3
18	2570.4	3445.8	390.1	237.1	2078.8	3170.6	3066.9	3752.8
19	1870.2	7328.7	365.9	638.6	1574.0	6575.5	2188.8	8088.1
20	2323.0	3297.9	894.4	410.7	1619.3	2799.8	3987.0	3859.1
21	2039.8	1725.8	115.5	176.9	1890.7	1490.8	2191.9	1945.1
22	2123.4	4715.2	202.9	365.9	1886.1	4287.5	2381.1	5132.5
23	2637.9	6592.1	337.2	448.8	2277.7	6014.4	3012.1	7194.9
24	2662.4	2475.3	533.5	438.2	2078.5	1876.6	3340.3	3039.1
25	2720.1	5220.1	861.0	840.5	1571.9	4104.4	3767.8	6308.2
26	2117.2	2397.2	260.9	326.6	1864.8	1999.1	2400.9	2804.5
27	2419.1	3869.8	201.3	391.1	2200.1	3399.3	2669.7	4386.8
28	1490.5	2852.3	100.1	349.4	1358.4	2373.0	1615.8	3285.0
29	2865.0	4719.0	246.5	294.1	2578.1	4338.2	3168.8	5099.9
30	3450.5	4377.7	353.8	221.8	3008.5	4093.5	3866.7	4654.6
31	1911.1	1982.9	125.9	238.7	1766.1	1705.2	2054.5	2310.6
32	1705.2	1112.0	138.1	338.8	1530.1	714.6	1888.6	1509.1
33	1165.6	1034.8	131.9	187.1	999.3	832.1	1324.6	1247.2
34	1775.2	2895.4	207.3	460.6	1541.5	2249.7	2036.3	3470.9
35	1953.7	6083.0	241.6	397.9	1631.6	5562.3	2251.7	6567.6
36	2228.4	5162.1	194.8	497.5	2029.0	4598.8	2450.8	5807.8
37	2840.6	1952.7	256.4	389.7	2527.8	1465.6	3168.2	2476.4
38	1967.8	1986.8	236.5	110.1	1696.1	1850.1	2277.1	2127.9

Table 13. RMS error of fitting eligible spokes to the ellipses in Table 12.

Subject	Mean Error (carotid)	Mean Error (jugular)	STD Error (carotid)	STD Error (jugular)	10th percentile Error (carotid)	10th percentile Error (jugular)	90th percentile Error (carotid)	90th percentile Error (jugular)
1	0.0137	0.0056	0.0068	0.0021	0.0069	0.0032	0.0222	0.0083
2	0.0134	0.0122	0.0067	0.0087	0.0073	0.0036	0.0196	0.0212
3	0.0373	0.0121	0.0155	0.0053	0.0194	0.0062	0.0606	0.0198
4	0.0316	0.0154	0.0132	0.0065	0.0190	0.0093	0.0510	0.0223
5	0.0452	0.0190	0.0154	0.0077	0.0245	0.0090	0.0700	0.0292
6	0.0301	0.0047	0.0097	0.0031	0.0188	0.0024	0.0430	0.0077
7	0.0371	0.0104	0.0136	0.0066	0.0206	0.0041	0.0550	0.0200
8	0.0440	0.0084	0.0172	0.0036	0.0223	0.0047	0.0700	0.0130
9	0.0280	0.0123	0.0072	0.0048	0.0198	0.0065	0.0370	0.0186
10	0.0109	0.0079	0.0042	0.0037	0.0061	0.0043	0.0166	0.0122
11	0.0184	0.0103	0.0057	0.0064	0.0123	0.0070	0.0255	0.0122
12	0.0228	0.0181	0.0093	0.0184	0.0129	0.0047	0.0352	0.0457
13	0.0453	0.0094	0.0136	0.0039	0.0277	0.0057	0.0645	0.0137
14	0.0241	0.0134	0.0094	0.0092	0.0138	0.0076	0.0367	0.0240
15	0.0186	0.0178	0.0069	0.0099	0.0117	0.0067	0.0261	0.0309
16	0.0342	0.0139	0.0232	0.0073	0.0100	0.0049	0.0700	0.0240
17	0.0169	0.0113	0.0057	0.0033	0.0106	0.0077	0.0242	0.0155
18	0.0321	0.0153	0.0150	0.0053	0.0154	0.0098	0.0530	0.0227
19	0.0168	0.0186	0.0089	0.0070	0.0085	0.0086	0.0249	0.0270
20	0.0215	0.0096	0.0135	0.0049	0.0093	0.0048	0.0419	0.0175
21	0.0138	0.0108	0.0064	0.0037	0.0070	0.0067	0.0230	0.0154
22	0.0308	0.0182	0.0128	0.0050	0.0151	0.0118	0.0486	0.0239
23	0.0183	0.0112	0.0070	0.0035	0.0108	0.0069	0.0272	0.0162
24	0.0329	0.0168	0.0152	0.0097	0.0143	0.0076	0.0547	0.0306
25	0.0304	0.0081	0.0150	0.0046	0.0140	0.0045	0.0519	0.0131
26	0.0181	0.0150	0.0097	0.0118	0.0085	0.0038	0.0317	0.0330
27	0.0136	0.0318	0.0082	0.0096	0.0061	0.0197	0.0245	0.0448
28	0.0095	0.0379	0.0041	0.0147	0.0049	0.0221	0.0143	0.0604
29	0.0128	0.0133	0.0072	0.0061	0.0062	0.0071	0.0210	0.0223
30	0.0355	0.0148	0.0092	0.0036	0.0244	0.0110	0.0476	0.0201
31	0.0149	0.0126	0.0042	0.0041	0.0100	0.0083	0.0204	0.0180
32	0.0126	0.0177	0.0053	0.0110	0.0074	0.0070	0.0183	0.0330
33	0.0204	0.0176	0.0089	0.0120	0.0110	0.0071	0.0318	0.0345
34	0.0329	0.0208	0.0099	0.0075	0.0200	0.0115	0.0452	0.0305
35	0.0244	0.0130	0.0072	0.0049	0.0156	0.0081	0.0333	0.0202
36	0.0154	0.0053	0.0098	0.0041	0.0068	0.0027	0.0275	0.0079
37	0.0325	0.0306	0.0108	0.0092	0.0185	0.0195	0.0477	0.0434
38	0.0283	0.0123	0.0134	0.0044	0.0126	0.0070	0.0466	0.0173

Table 14. Vessel depth (mm) as approximated by the distance between the center of the fitted ellipses (Table 12) to the skin.

Subject	Mean Depth (carotid)	Mean Depth (jugular)	STD Depth (carotid)	STD Depth (jugular)	10th percentile Depth (carotid)	10th percentile Depth (jugular)	90th percentile Depth (carotid)	90th percentile Depth (jugular)
1	207.9	178.8	9.36	5.34	200.2	174.3	222.3	188.3
2	247.0	174.4	6.21	4.33	239.5	170.4	255.7	179.5
3	307.5	185.9	3.87	2.94	302.8	182.3	312.3	190.0
4	169.8	134.1	2.72	1.19	166.5	132.8	173.2	135.2
5	288.3	200.6	10.69	8.47	278.2	193.8	303.1	209.1
6	275.9	170.1	10.55	6.91	261.4	160.5	289.6	179.1
7	339.3	234.2	5.57	3.42	332.8	229.6	346.6	237.2
8	298.6	189.9	4.56	1.97	292.9	187.7	303.8	192.2
9	248.2	181.2	3.57	1.09	243.9	179.9	252.7	182.6
10	284.7	183.8	2.13	1.85	282.0	181.7	287.4	185.9
11	273.7	169.5	6.58	3.35	265.1	165.1	282.4	173.7
12	249.6	163.5	5.37	7.74	242.8	156.9	255.9	175.3
13	249.7	176.1	5.21	2.97	243.1	172.2	256.2	180.0
14	225.4	145.6	3.61	2.39	220.8	143.2	230.1	147.8
15	192.2	142.0	5.37	4.50	186.7	137.4	199.1	147.1
16	151.3	96.7	5.96	2.90	143.8	92.9	158.9	100.5
17	284.6	166.8	5.07	2.06	278.7	164.0	290.8	169.5
18	204.4	136.4	3.56	1.74	200.4	134.2	208.6	138.7
19	270.3	167.3	7.85	4.17	261.6	162.2	277.9	170.7
20	255.6	161.5	4.97	1.94	249.2	159.0	261.9	164.1
21	209.3	147.0	2.13	1.28	206.4	145.4	211.9	148.6
22	272.4	181.9	3.65	2.47	267.2	179.3	276.5	184.6
23	248.9	155.8	9.84	7.80	240.3	149.8	266.5	170.8
24	221.5	157.2	5.24	5.48	214.0	149.0	228.0	162.9
25	262.3	161.6	11.83	4.57	246.1	155.6	278.7	168.2
26	204.6	131.8	5.07	2.96	199.1	127.6	212.3	135.4
27	229.0	162.8	3.24	2.66	225.9	159.4	231.2	165.2
28	224.5	182.5	2.14	3.33	221.9	178.2	227.6	187.0
29	224.8	147.9	3.35	1.52	220.1	146.0	229.2	149.7
30	210.2	125.9	4.62	1.48	204.3	124.1	215.3	127.6
31	202.4	136.5	2.69	1.28	199.2	134.7	205.8	138.1
32	216.9	144.9	2.13	1.84	214.4	142.8	219.2	147.1
33	170.7	138.8	6.50	6.78	161.7	130.2	178.8	147.1
34	243.3	166.1	3.94	2.01	238.1	163.8	248.5	168.6
35	259.5	147.0	5.03	3.75	253.4	141.9	265.0	150.8
36	228.0	163.0	3.80	2.43	223.7	160.9	233.0	165.3
37	185.6	109.6	5.28	3.90	177.8	104.4	191.8	114.3
38	145.6	96.9	4.03	0.82	141.2	95.9	151.6	97.9

Table 15. Eccentricity of the fitted ellipses.

Subject	Mean Eccentricity (carotid)	Mean Eccentricity (jugular)	STD Eccentricity (carotid)	STD Eccentricity (jugular)	10^{th} percentile Eccentricity (carotid)	10th percentile Eccentricity (jugular)	90th percentile Eccentricity (carotid)	90th percentile Eccentricity (jugular)
1	0.613	0.803	0.068	0.028	0.533	0.767	0.686	0.837
2	0.599	0.574	0.058	0.095	0.521	0.442	0.664	0.684
3	0.647	0.590	0.165	0.066	0.419	0.503	0.843	0.661
4	0.655	0.734	0.075	0.097	0.558	0.611	0.741	0.836
5	0.686	0.583	0.131	0.082	0.489	0.477	0.821	0.683
6	0.729	0.680	0.080	0.058	0.621	0.606	0.808	0.753
7	0.566	0.728	0.145	0.054	0.373	0.654	0.739	0.789
8	0.645	0.613	0.136	0.048	0.482	0.549	0.810	0.665
9	0.466	0.645	0.112	0.061	0.318	0.565	0.604	0.716
10	0.462	0.662	0.124	0.049	0.308	0.599	0.621	0.721
11	0.617	0.663	0.069	0.048	0.528	0.596	0.701	0.717
12	0.632	0.624	0.130	0.108	0.450	0.495	0.779	0.766
13	0.626	0.599	0.125	0.067	0.458	0.510	0.771	0.664
14	0.749	0.562	0.084	0.058	0.641	0.488	0.826	0.625
15	0.478	0.794	0.110	0.046	0.329	0.744	0.614	0.842
16	0.847	0.710	0.069	0.064	0.770	0.615	0.909	0.790
17	0.682	0.553	0.113	0.056	0.527	0.476	0.803	0.629
18	0.710	0.538	0.089	0.096	0.593	0.414	0.798	0.642
19	0.701	0.669	0.093	0.083	0.579	0.555	0.809	0.766
20	0.631	0.758	0.139	0.055	0.456	0.676	0.798	0.811
21	0.689	0.772	0.046	0.038	0.627	0.729	0.747	0.815
22	0.702	0.693	0.090	0.059	0.575	0.616	0.782	0.759
23	0.694	0.592	0.087	0.067	0.587	0.506	0.786	0.672
24	0.790	0.750	0.062	0.072	0.702	0.661	0.862	0.823
25	0.713	0.675	0.132	0.042	0.533	0.623	0.862	0.721
26	0.704	0.744	0.064	0.094	0.638	0.612	0.775	0.840
27	0.764	0.655	0.057	0.075	0.718	0.565	0.814	0.734
28	0.565	0.691	0.063	0.091	0.487	0.579	0.637	0.798
29	0.750	0.736	0.044	0.043	0.702	0.678	0.804	0.788
30	0.505	0.798	0.108	0.025	0.360	0.769	0.622	0.821
31	0.741	0.709	0.054	0.050	0.679	0.651	0.801	0.782
32	0.633	0.738	0.052	0.086	0.567	0.632	0.697	0.831
33	0.631	0.648	0.084	0.093	0.524	0.540	0.725	0.754
34	0.711	0.713	0.073	0.057	0.628	0.641	0.796	0.789
35	0.714	0.627	0.100	0.063	0.570	0.540	0.819	0.705
36	0.653	0.853	0.065	0.030	0.586	0.824	0.721	0.887
37	0.702	0.695	0.064	0.096	0.611	0.578	0.779	0.793
38	0.720	0.769	0.112	0.033	0.568	0.720	0.846	0.803

Table 16. Heart rate and respiratory rate derived from Fourier transform of the fitted ellipse time series

Subject	Heart Rate (carotid)	Heart Rate (jugular)	Heart Rate Strength (carotid)	Heart Rate Strength (jugular)	Respiratory Rate (carotid)	Respiratory Rate (jugular)	Respiratory Rate Strength (carotid)	Respiratory Rate Strength (jugular)
1	58.1	59.4	25290	25169	16.8	15.5	8343	21942
2	72.2	72.2	9600	53491	17.8	18.9	5858	50393
3	56.7	56.7	21466	24583	13.3	11.1	22814	28711
4	67.9	67.9	23578	46183	16.0	20.0	11042	14221
5	59.4	72.6	16153	40513	21.1	21.1	23587	22274
6	72.5	72.5	28185	103174	17.1	18.4	25008	35749
7	63.0	63.0	47724	129831	15.7	10.5	22938	61719
8	59.5	59.5	33034	63494	10.6	22.5	19419	27630
9	52.8	54.1	29746	54192	15.8	14.5	6356	25102
10	49.0	49.0	38789	20002	10.6	18.6	14161	11124
11	49.0	49.0	34056	82900	10.6	22.5	11311	39609
12	54.1	52.8	37639	59464	14.5	11.9	21989	72920
13	67.9	61.2	18849	56320	22.6	26.6	22525	24138
14	67.4	67.4	19709	26063	21.2	10.6	14509	65852
15	60.7	60.7	7495	36348	10.6	21.1	6903	12280
16	42.8	58.9	21289	37907	17.4	17.4	35593	22082
17	54.3	54.3	21610	35176	13.9	21.9	19917	42341
18	47.1	47.1	44299	19973	17.2	17.2	25608	14942
19	61.0	64.6	15433	59903	19.9	19.2	23630	47956
20	59.3	61.4	19743	56844	16.2	20.5	30921	19446
21	67.4	70.4	10473	19300	16.5	15.7	7700	9712
22	56.6	66.5	9075	26383	24.1	23.4	11013	14998
23	78.1	80.2	22890	28152	17.0	18.4	16854	21773
24	66.7	66.0	21029	43060	11.4	20.6	29248	31783
25	67.5	68.2	25636	121166	9.7	22.3	31560	36131
26	75.5	75.5	13248	28886	10.0	19.2	16175	17275
27	65.6	65.6	16976	50432	12.0	19.8	8664	26102
28	51.8	63.8	11073	14812	13.5	13.5	6751	17039
29	61.2	61.2	25211	32134	22.7	11.3	8337	23630
30	65.2	65.2	12431	20702	20.5	19.7	31081	20783
31	65.1	62.9	7871	31786	12.9	12.9	6913	12221
32	64.4	64.4	19649	48196	17.4	15.9	5287	20000
33	54.7	54.7	12303	10981	14.4	14.4	4135	10518
34	54.6	64.5	8613	24582	17.4	18.2	15028	38716
35	60.8	60.8	14024	31988	25.1	25.1	34240	21152
36	59.4	57.1	11481	43806	28.9	18.3	10927	21322
37	49.2	49.2	17984	40946	22.0	18.2	14678	29272
38	82.7	81.9	10075	7157	11.4	20.5	9542	12201

Table 17. Compliance measure, phase differences, and phase consistency.

Subject	Fourier Slope (carotid)	Fourier Slope (jugular)	Phase shift between carotid and jugular	Phase consistency between carotid and jugular
1	-7	-10	-2.89	0.89
2	-10	-76	-2.27	0.74
3	-12	-20	-2.82	0.28
4	-14	-26	-1.90	0.63
5	-12	-36	2.50	0.47
6	-21	-74	3.08	0.79
7	-21	-57	-2.51	0.65
8	-17	-36	-2.78	0.64
9	-8	-8	-2.55	0.85
10	-11	-8	-2.98	0.68
11	-9	-17	-2.64	0.56
12	-9	-30	-2.43	0.39
13	-14	-43	2.90	0.87
14	-15	-36	-2.45	0.55
15	-5	-25	-2.36	0.80
16	-12	-8	-2.08	0.26
17	-9	-24	-3.10	0.46
18	-16	-9	-2.74	0.59
19	-28	-74	-3.06	0.77
20	-44	-33	-2.61	0.43
21	-14	-19	-2.18	0.83
22	-5	-42	1.08	0.00
23	-1	-20	1.64	0.29
24	-21	-34	-1.09	0.62
25	-23	-74	-1.86	0.46
26	-15	-29	-2.50	0.78
27	-15	-46	-2.12	0.76
28	-15	-25	-2.50	0.75
29	-28	-32	-2.69	0.78
30	-9	-31	-1.62	0.35
31	-16	-33	-1.22	0.79
32	-16	-68	-2.20	0.97
33	-24	-15	-3.14	0.88
34	-14	-43	3.12	0.58
35	-9	-34	-2.07	0.46
36	-26	-73	-2.50	0.53
37	-28	-70	-2.47	0.78
38	-15	-10	-2.65	0.45

References

1. Davies MJ, Cronin KD, and Domaingue CM Pulmonary artery catheterization: an assessment of risks and benefits in 220 surgical patients. Anaesth Intensive Care 10:9, 1982.
2. Patel C; Laboy V; Venus B; Mathru M; Wier D Acute complications of pulmonary artery catheter insertion in critically ill patients. Crit Care Med, 14(3):195-7 1986 Mar
3. Knoblanche GE Respiratory obstruction due to haematoma following internal jugular vein cannulation. Anaesth Intensive Care 7: 286, 1979
4. Kua JS; Tan IK Airway obstruction following internal jugular vein cannulation. Anaesthesia, 52:776-80, 1997
5. Shield CF, Richardson JD, Buckley CJ et al: Pseudoaneurysm of the brachiocephalic arteries: A complication of percutaneous internal jugular vein catheterization. Surgery 78:190-193, 1975
6. Aoki H. Mizobe T. Nozuchi S. et al: Vertebral artery pseudoaneurysm: A rare complication of internal jugular vein catheterization. Anesth Analg 75:296-298,1992
7. Gobeil F. Couture P. Girard D, Plante R: Carotid Artery-lnternal Jugular Fistula: Another Complication following Pulmonary Artery Catheterization via the Internal Jugular Venous Route. Anesthesiology 1994, 80:23-232.
8. Applebaum RM, Adelman MA, Kanschuger MS, Jacobowitz G, Kronzon I Transesophageal echocardiographic identification of a retrograde dissection of the ascending aorta caused by inadvertent cannulation of the common carotid artery. J Am Soc Echocardiogr 1997 Sep;10(7):749-51
9. Zaidi NA, Khan M, Naqvi HI, Kamal RS Cerebral infarct following central venous cannulation. Anaesthesia, 53:186-91, 1998 Feb
10. Sulek CA, Gravenstein N, Blackshear RH, Weiss L: Head rotation during internal jugular vein cannulation and the risk of carotid artery puncture. Anesth Analg 1996; 82: 125-128
11. Denys BG, Uretsky BF: Anatomical variations of internal jugular vein location: impact on central venous access. Crit Care Med 1991; 19: 1516-1519
12. Alderson PJ, Burrows FA, Stemp LI , Holtby HM: Use of ultrasound to evaluate internal jugular vein anatomy and to facilitate central venous cannulation in paediatric patients. Br J Anaesth 1993; 70: 145-148
13. Denys BG et al, "Ultrasound-assisted cannulation of the internal jugular vein: A prospective comparison to the external landmark-guided technique," *Circulation* 1993; 87:1557-62.
14. P. Abolmaesumi, M. Sirouspour, and S. Salcudean, "Real-Time Extraction of Carotid Artery Contours from Ultrasound Images" 13th IEEE Symposium on Computer-Based Medical Systems (CBMS'00) p. 181
15. F. Yeung, S. F. Levinson, D. Fu, and K. J. Parker, "Feature-Adaptive Motion Tracking of Ultrasound Image Sequences Using A Deformable Mesh" IEEE Transactions on Medical Imaging Vol. 17, No. 6, Dec 1998
16. Nakayama K and Sato S, "Ultrasonic measurement of arterial wall movement utilizing phase-tracking systems," *Proceedings of the 10th International Congress on Medical and Biological Engineering*, Dresden, Germany, 1973:318. Abstract

17. L. S. Wilson, M. J. Dadd, and R. W. Gill, "Automatic vessel tracking and measurement for Doppler studies," *Ultrasound Med Biol*. 1990;16(7):645-52
18. K. Drukker, M. L. Giger, K. Horsch, M. A. Kupinski, C. J. Vyborny, and E. B. Mendelson, "Computerized lesion detection on breast ultrasound," *Medical Physics*, July 2002, Volume 29, Issue 7, pp. 1438-1446
19. H. M. Ladak, F. Mao, Y. Wang, D. B. Downey, D. A. Steinman, and A. Fenster, "Prostate boundary segmentation from 2D ultrasound images" *Medical Physics*, August 2000, Volume 27, Issue 8, pp. 1777-1788
20. K. J. Draper, C. C. Blake, L. Gowman, D. B. Downey, A. Fenster, "An algorithm for automatic needle localization in ultrasound-guided breast biopsies," *Medical Physics*, August 2000, Volume 27, Issue 8, pp. 1971-1979
21. Rosenthal M, State A, Lee J et al. Augmented reality guidance for needle biopsies: an initial randomized, controlled trial in phantoms. Med Image Anal 2002;6(3):313-20.
22. Sauer F, Khamene A, Bascle B, Schimmang L, Wenzel F, Vogt S. Augmented reality visualization of ultrasound images: System description, calibration, and features. In: 4th International Symposium on Augmented Reality - ISAR; 2001 October; New York, NY: IEEE, ACM; 2001. p. 30-9.
23. Fuchs H, State A, Pisano ED et al. Towards Performing Ultrasound-Guided Needle Biopsies from within a Head-Mounted Display. In: Visualization in Biomedical Computing; 1996 September 22-25, 1996; Hamburg, Germany; 1996. p. 591-600.
24. State A, Livingston MA, Garrett WF et al. Technologies for Augmented Reality Systems: Realizing Ultrasound-Guided Needle Biopsies. In: SIGGRAPH; 1996; New Orleans, LA: ACM Press; 1996. p. 429-38.
25. S. Clanton, D. Wang, Y. Matsuoka, D. Shelton, G. Stetten, Novel machine interface for scaled telesurgery, SPIE Medical Imaging, vol. 5367, pp. 697-704., San Diego, Feb. 2004
26. S. Clanton, D. Wang, V. Chib, Y. Matsuoka, G. Stetten, Optical Merger of Direct Vision with Virtual Images for Scaled Teleoperation, IEEE Transactions on Visualization and Computer Graphics (TVCG), Vol. 12, No. 2, March/April 2006
27. Birkfellner, W., Figl, M., Huber, K., Watzinger, F., Wanschitz, F., hanel, R., Wagner, A., Rafolt, D., Ewers, R. & Bergmann, H., The Varioscope AR - A head-mounted operating microscope for augmented reality. (Medical image Computing and Computer-Assisted Intervention (MICCAI), Springer, Pittsburgh) Lecture Notes in Computer Science, 1935 869-877 (2000).
28. Edwards, P. J., Hawkes, D. J. & Hill, D. L., Augmentation of reality using an operating microscope for otolaryngology and neurosurgical guidance. J Image Guid Surg 1, 172-178 (1995).
29. Nelson, B. J. & Vikramaditya, B., Visually servoed micropositioning for robotic micromanipulation. Microcomputer Applications 18, 23-31 (1999).
30. G. Stetten, V. Chib, "Magnified Real-Time Tomographic Reflection," Medical Image Computing and Computer-Assisted Intervention – MICCAI 2001. Lecture Notes in Computer Science , vol. 2208, pp. 683-690, 2001
31. Frank H. Netter, Atlas of Human Anatomy (2ed), ICON Learning Systems, NJ, 2001: p26
32. Leonard S. Lilly, Pathophysiology of Heart Disease (3ed), Lippincott Willaims & Wilkins, Baltimore, MD,, 2003; 30

33. Constant J. "Jugular wave recognition breakthrough. X' descent vs the X descent and trough." Chest 2000; 118:1788-1791.
34. D. Wang, R. Klatzky, N. Amesur, and G. Stetten, Carotid Artery and Jugular Vein Tracking and Differentiation Using Spatiotemporal Analysis, Medical Image Computing and Computer-Assisted Intervention (MICCAI 2006), Lecture Notes in Computer Science, vol. 4190, pp. 654-661
35. D. Wang, W. Chang, G. Stetten, Real-Time Ultrasound Image Analysis for the Insight Toolkit, Technical report in special MICCAI 2005 Workshop on Open-Source Software issue of The Insight Journal
36. Pilu M, Fitzgibbon A, Fisher R, "Ellipse-specific direct least-square fitting," Proceedings of the IEEE international Conference on Image Processing, IEEE Computer Society Press, Los Alamitos, CA 1996; 3:599-602
37. A. Zijdenbos, B. Dawant, and R. Marjolin, "Morphometric analysis of white matter lesions in MR images: Methods and validation," IEEE TMI, vol. 13(4), pp. 716–724, 1994
38. D. Poxton, J. Graham, and J. F. W. Deakin, "Detecting asymmetries in hippocampal shape and receptor distribution using statistical appearance models and linear disciminant analysis," *Britich mashine vision conference*, pp. 525-534, 1998.
39. C. A. Troianos, R. J. Kuwik, J. R. Pasqual, A. J. Lim, D. P. Odasso, "Internal Jugular Vein and Carotid Artery Anatomic Relation as Determined by Ultrasonography," *Anesthesiology* 1996; 85:43-8
40. D. Wang, B. Wu, G. Stetten, A Laser Needle Guide for the Sonic Flashlight, Medical Image Computing and Computer-Assisted Intervention Conference, Oct. 26-29, 2005, Palm Springs, CA
41. Reid MH. Real-time sonographic needle biopsy guide. Am J Roentgenol 1983;140(1):162-3.
42. Yeh HC, Mitty HA, Wolf BS. A simple ultrasound guide for needle puncture. J Clin Ultrasound 1976;4(1):53-4.
43. Lindgren PG, Hemmingsson A. Percutaneous nephropyelostomy. A new technique. Acta Radiol Diagn (Stockh) 1980;21(6):759-61.
44. Lindgren PG. Ultrasonically guided punctures. A modified technique. Radiology 1980;137(1 Pt 1):235-7.
45. Han D, Lan Seo Y, Soon Choi C et al. A steerable guiding device: the new method in ultrasound guidance. Invest Radiol 2002;37(11):626-31.
46. O. Chavanon, C. Barbe, J. Troccaz, L. Carrat, and D. Ribuot, C. aand Blin. Accurate guidance for percutaneous access to a specific target in soft tissues. Journal of Laparoendoscopic and advanced surgical techniques, 9(3):259-266, 1999.
47. 7. S. Nicolau, A. Garcia, X. Pennec, L. Soler, N. Ayache An Augmented Reality system to guide radio-frequency tumor ablation Journal of Computer Animation and Virtual World, 2005, Vol. 16(1), p1-10.
48. D. Wang, NB. Amesur, D. Weiser, WM. Chang, AB. Zajko, G. Stetten. Improving Image Quality of the Sonic Flashlight for Venous Access. 107th annual meeting of the American Roentgen Ray Society, Abstract no. 1135, May 6-11, 2007, Orlando, FL.
49. W. Chang, N. Amesur, D. Wang, A. Zajko, G. Stetten. First Clinical Trial of the Sonic Flashlight - Guiding Placement of Peripherally Inserted Central Catheters, 2005

meeting of the Radiological Society of North America, November 2005, Chicago, Illinois. Paper Number SSJ03-02
50. S. Clanton, D. Wang, Y. Matsuoka, D. Shelton, G. Stetten. Novel machine interface for scaled telesurgery, SPIE Medical Imaging, vol. 5367, pp. 697-704., San Diego, Feb. 2004
51. S. Clanton, D. Wang, V. Chib, Y. Matsuoka, G. Stetten, Optical Merger of Direct Vision with Virtual Images for Scaled Teleoperation, IEEE Transactions on Visualization and Computer Graphics (TVCG), Vol. 12, No. 2, March/April 2006
52. A. Nowatzyk, D. Shelton, J. Galeotti, G. Stetten, "Extending the Sonic Flashlight to Real Time Tomographic Holography," AMI-ARCS 2004, Workshop for Augmented environments for Medical Imaging including Augmented Reality in Computer-aided Surgery, Rennes, France, September 30, 2004
53. Douglas Christensen, Ultrasound Bioinstrumentation, John Wiley and Sons, 1988.
54. W. Chang, N. Amesur, D. Wang, A. Zajko, G. Stetten, "First Clinical Trial of the Sonic Flashlight – Guiding Placement of Peripherally Inserted Central Catheters," 2005 meeting of the Radiological Society of North America, November 2005, Chicago, Illinois. Paper Number SSJ03-02.
55. G. Stetten, A. Cois, W. Chang, D. Shelton, R. Tamburo, J. Castellucci, O. von Ramm, "C-mode Virtual Image Display for a Matrix Array Ultrasound Sonic Flashlight," Medical Image Computing and Computer-Assisted Intervention – MICCAI 2003. Lecture Notes in Computer Science, vol. 2879, pp. 336-343.
56. G. Stetten, A. Cois, W. Chang, D. Shelton, R. Tamburo, J. Castellucci, O. von Ramm, "C-mode Virtual Image Display for a Matrix Array Ultrasound Sonic Flashlight," (1 of 12 papers from MICCAI, invited to be in a special issue of Academic Radiology, in press).
57. G. Shukla, B. Wu, D. Schwartzman, G., Stetten, "The Sonic Penlight for Guidance of Superficial Subdermal Access," Medical Image Computing and Computer-Assisted Intervention Conference, Oct. 26-29, 2005, Palm Springs, FL (# 542).
58. D. Wang, B. Wu, G. Stetten, "A Laser Needle Guide for the Sonic Flashlight," Medical Image Computing and Computer-Assisted Intervention Conference, Oct. 26-29, 2005, Palm Springs, CA (# 181).
59. G. Stetten, V. Chib, "Magnified Real-Time Tomographic Reflection," Medical Image Computing and Computer-Assisted Intervention – MICCAI 2001. Lecture Notes in Computer Science, vol. 2208, pp. 683-690, 2001. S. Clanton, D. Wang, Y. Matsuoka, D. Shelton, G. Stetten, "Novel machine interface for scaled telesurgery," SPIE Medical Imaging, vol. 5367, pp. 697-704., San Diego, Feb. 2004.
60. S. Clanton, D. Wang, V. Chib, Y. Matsuoka, G. Stetten, "Optical Merger of Direct Vision with Virtual Images for Scaled Teleoperation," IEEE Transactions on Visualization and Computer Graphics (TVCG), Vol. 12, No. 2, March/April 2006.
61. D. Wang, R. Klatzky, N. Amesur, George Stetten, "Carotid Artery and Jugular Vein Tracking and Differentiation using Spatiotemporal Analysis," MICCAI 2006, Lecture Notes in Computer Science, vol. 4190, pp. 654-661.
62. D. Shelton, R. Klatzky, G. Stetten, "Method for assessing augmented reality needle guidance using a virtual biopsy task," Abstracts of the IEEE International Symposium on Biomedical Imaging, p.. 13, April, 2004, Arlington, VA.

63. G. Stetten, A. Nowatzyk, “Combining Tomographic Images in situ with Direct Vision Using a Holographic Optical Element,” US Patent Application no. 20030199765, Continuation in Part to Patent no. 6,599,247, (2001).
64. G. Stetten, A. Nowatzyk, D. Shelton, “Augmenting visual Perception with Real-Time Tomographic Holography,” 2003 NSF Principle Investigator Workshop on Robotics and Computer Vision, Las Vegas, Nevada, October 26-27, 2003.
65. A. Nowatzyk, D. Shelton, J. Galeotti, G. Stetten, “Extending the Sonic Flashlight to Real Time Tomographic Holography,” AMI-ARCS 2004, Workshop for Augmented environments for Medical Imaging including Augmented Reality in Computer-aided Surgery, Rennes, France, September 30, in conjunction with MICCAI 2004.
66. J. Galeotti, ”A system for in situ tomographic visualization by use of near-field holographic virtual image projection, Ph.D. Thesis Proposal, The Robotics Institute, Carnegie Mellon University, May 3, 2006. Committee: G. Stetten (chair), M. Siegel, R. Klatzky, M. Hebert.
67. R. Klatzky, B. Wu, D. Shelton, G. Stetten, “Efficacy of Image-Guided Action is Controlled by Perception,” Vision Sciences Society Meeting, 2005, Sarasota, FL., May 6-11, 2005.
68. B. Wu, R. Klatzky, D. Shelton, G. Stetten, “Psychophysical Evaluation of In-Situ Ultrasound Visualization”, IEEE Transactions on Visualization and Computer Graphics (TVCG), Special Issue on Haptics, Virtual and Augmented Reality, November/December Issue, pp. , 684-693, 2005.
69. B. Wu, R. Klatzky, D. Shelton, G. Stetten, “Interaction of Visual and Haptic Cues in the Image-based Perception of Depth,” Vision Sciences Society Meeting, 2006, Sarasota, FL., May 5-10, 2006 (abstract VSS#284).
70. R. Klatzky, B. Wu, D. Shelton, and G. Stetten, “Superiority of In-situ Ultrasound Visualization for Medical Intervention when Action Varies," Haptic Interfaces for Virtual Environment and Teleoperator Systems, IEEE Virtual Reality 2006, Arlington VA, 25-26 March 2006 (poster presentation only – not published in proceedings).
71. R. Klatzky, B. Wu, D. Shelton, G. Stetten, “Effectiveness of Augmented-Reality Visualization vs. Cognitive Mediation for Learning Actions in Near Space,” ACM Transactions in Applied Perception, (submitted).
72. W. Chang, Guiding Vascular Access with the Sonic Flashlight - Preclinical Development and Validation, Ph.D. Dissertation, Department of Bioengineering, University of Pittsburgh, Aug. 5, 2004
73. G. Stetten, V. Chib, D. Hildebrand, J. Bursee, Real Time Tomographic Reflection: Phantoms for Calibration and Biopsy, Proceedings of the IEEE and ACM International Symposium on Augmented Reality, New York City, Oct 29-30, 2001, pp. 11-18.